12 Aerosols and Clouds in the Climate System

Aerosol particles affect the climate directly by scattering solar radiation and by absorbing solar and terrestrial radiation, as discussed in Chapter 2, referred to as aerosol–radiation interactions. In addition, aerosol particles can affect the climate indirectly by modifying cloud microphysical and radiative properties when acting as CCN (Chapter 7) and as INPs (Chapter 9), referred to as aerosol–cloud interactions. Aerosol radiative forcing, from human-driven aerosol–radiation and aerosol–cloud interactions, significantly impacts Earth's climate system. This has been documented by the scientific community in the assessment reports of the IPCC[1]. Here, we generally refer to the latest IPCC assessment report (AR6) as it builds upon the previous reports. The IPCC synthesizes the knowledge about natural and anthropogenic climate change, including all forcing agents.

Since AR5, the analysis of climate change is conceptualized into instantaneous radiative forcings, adjustments, and feedbacks. Here, the forcing describes the perturbation of the Earth energy budget, whereas the adjustments and feedbacks denote the response of the climate system to the forcing. The impact of the different forcing agents is commonly expressed in terms of their *instantaneous radiative forcing* (IRF) in $\mathrm{W\,m^{-2}}$. IRF is defined as the imbalance of Earth's energy budget, which results from an external perturbation (or forcing) of the climate system. Perturbations can be natural or anthropogenic in origin: natural perturbations include changes in solar activity and volcanic eruptions that release CO_2 and aerosol particles into the atmosphere, whereas anthropogenic perturbations include emissions of greenhouse gases and aerosol particles due to industrial activity and biomass burning. IRF is calculated as the difference in the TOA net radiative flux between two radiative transfer calculations that differ only by the amount of the forcing agent under consideration. A positive IRF leads to a warming and a negative IRF to a cooling of the Earth-atmosphere system.

The *effective radiative forcing* (ERF) includes this IRF plus the subsequent *rapid adjustments* in the climate system, which act independently of Earth's global mean surface temperature change (Sherwood et al., 2015; Forster et al., 2021). Adjustments include, for instance, changes in stratospheric temperature, cloud cover, cloud liquid water, and cloud ice content, in response to the initial perturbation (Quaas et al., 2024), as schematically visualized in Figure 12.1. These occur rapidly, on timescales of hours to days for adjustments in clouds, to weeks to several months for adjustments in stratospheric temperatures, all of which are much shorter than the lifetimes of WMGHG (Hansen et al., 1997; Myhre et al., 1998). Adjustments can either enhance or dampen a given IRF. ERF gives a more accurate estimate of the final

[1] www.ipcc.ch/reports/

https://doi.org/10.1017/9781009485654.013 Published online by Cambridge University Press

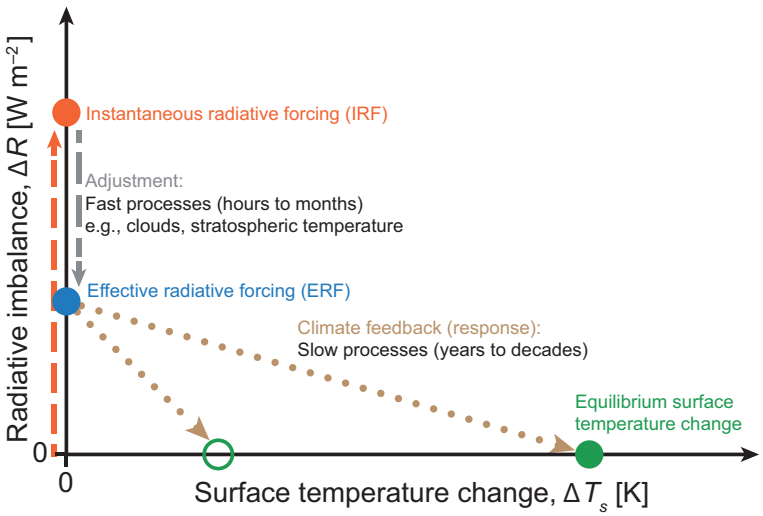


Figure 12.1 Diagram showing a climate perturbation causing a radiative imbalance ΔR, and a change in global surface temperature ΔT_s, to illustrate the relation between IRF, ERF, and climate response. The IRF is depicted as a positive value and denotes the initial radiative imbalance with respect to a reference state. ERF is the superposition of the IRF and adjustments, which do not (immediately) affect globally averaged surface temperature. For the system to return to radiative balance at a new equilibrium, the surface temperature has to adjust. Figure based on Bellouin et al. (2020).

impact of forcing agents on climate as compared to IRF. These aspects are further discussed in Section 12.1.

Clouds have a large effect on Earth's energy budget. Their climate impact depends on the altitude and the geographical locations where they form. These two aspects have been introduced in Chapter 2. Trends in cloud cover will be discussed in Section 12.2.

The increase in GHGs causes the temperature of Earth's atmosphere to increase. In addition to the IRF and associated (rapid) adjustments, so-called *climate feedbacks* take place. In contrast to the adjustments, which occur at a constant global surface temperature, climate feedbacks describe slow processes that typically occur on time scales of years to decades and act in response to global-mean surface temperature T_s changes, and change T_s (Figure 12.1).

A prominent example of such a positive climate feedback is an increase in the water vapor mixing ratio due to the higher saturation water vapor pressure at higher temperature according to the Clausius–Clapeyron equation (eq. 3.70). Because water vapor is a GHG, that absorbs more radiation in the longwave than in the shortwave (Figure 2.1), an increase in water vapor further amplifies the warming and hence the surface temperature, which in turn increases the water vapor mixing ratio. Climate feedbacks associated with changes in cloud properties can be positive or negative, as will be discussed in Section 12.3.

Given that extinction of solar radiation by aerosol particles partly offsets GHG warming, it has been suggested that aerosol particles should be deliberately injected into the atmosphere to

https://doi.org/10.1017/9781009485654.013 Published online by Cambridge University Press

cool the climate either by directly modifying the energy budget (ERF due to aerosol–radiation interactions (ERFari)) or by changing cloud properties (ERF due to aerosol–cloud interactions (ERFaci)). This so-called *climate intervention* involving aerosol particles and clouds is discussed in Section 12.4.

12.1 Aerosol Radiative Forcing

The ERF for aerosols is the sum of ERFari and ERFaci, formerly called the direct and indirect effects of aerosols on climate, respectively. In the following, we will first discuss ERFari (Section 12.1.1) and ERFaci (Section 12.1.2) separately, before putting them in the context of ERF of other radiative forcings (Section 12.1.3).

12.1.1 Effective Radiative Forcing due to Aerosol–Radiation Interactions

The ERFari is proportional to the amount of aerosol particles in the atmosphere and to their ability to extinguish radiation by scattering and absorption (Chapter 2). Both are functions of the particle properties (e.g., size) and the wavelength of the electromagnetic radiation (Moosmüller et al., 2009).

Scattering and absorption of solar radiation by aerosol particles reduce the amount of solar radiation that can reach and be absorbed at Earth's surface and hence contribute to a negative IRF due to aerosol–radiation interactions (IRFari) at Earth's surface. Adjustments to scattering of solar radiation by aerosols include the spread of the cooling regionally and in the vertical direction. By contrast, absorption of solar radiation by black carbon (BC) causes a local heating in the atmosphere, that is, a positive IRFari. Over time, this heating is also felt at the surface, causing ERFari from BC to be positive both at TOA and at Earth's surface (Boucher et al., 2013).

Aerosol optical or radiative properties depend on their shapes, sizes, chemical compositions, and mixing states. Thus, scattering and absorbing properties can vary greatly for different aerosol particles and types. The scattering of solar radiation ($0.2 \leq \lambda \leq 4\,\mu m$) by aerosol particles is dominated by Mie scattering (Figure 2.2). The scattering efficiency is largest for aerosol particles that have diameters comparable to the wavelengths of the electromagnetic radiation with which they interact. For the scattering of visible light, this corresponds to accumulation mode aerosol particles ($0.05 \leq r \leq 0.5\,\mu m$, Table 6.1). In addition, some aerosol types, such as BC and brown carbon (Laskin et al., 2015, Section 6.1.1), also absorb solar radiation.

Overall, the shortwave ERFari is typically negative, since aerosol scattering prevails over absorption for most aerosol types. An exception is BC, which is highly absorptive in the shortwave and thus has a positive IRFari at TOA (Szopa et al., 2021). This is illustrated in Figure 12.2, which displays IRFari for different aerosol types (Myhre et al., 2013). IRFari can be determined from GCMs by calculating the radiative transfer equation twice, once with and once without the respective aerosol type.

Aerosol particles with sizes in the micrometer range tend to absorb more and scatter less radiation, both in the shortwave and the longwave spectrum. Hence, larger aerosol particles can have a considerable positive longwave ERFari. For instance, sulfate aerosol particles

https://doi.org/10.1017/9781009485654.013 Published online by Cambridge University Press

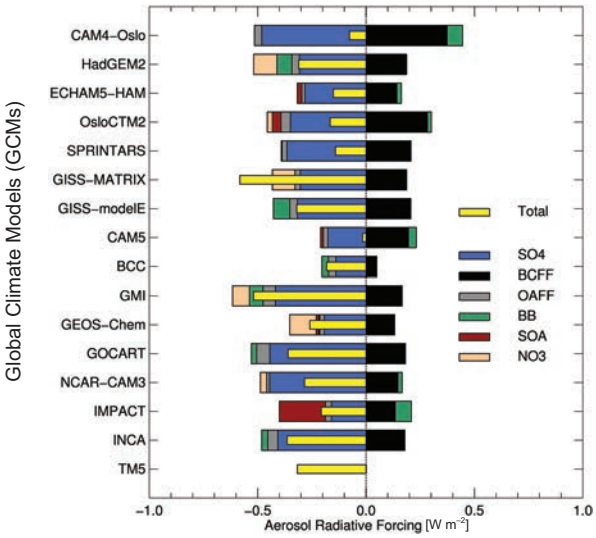


Figure 12.2 Simulated contributions of six anthropogenic aerosol types, sulfate aerosol particles (SO_4), Black carbon (BC) from fossil fuel combustion (BCFF), organic aerosols from fossil fuel combustion (OAFF), biomass burning (BB), Secondary organic aerosol (SOA), and nitrate (NO_3), to the aerosol IRFari together with the total IRFari from 16 global coupled aerosol-climate models. Figure adapted from Myhre et al. (2013).

exhibit a net negative ERFari as long as they are smaller than 2 μm and a net positive ERFari at larger radii (Lacis et al., 1992). In the global annual mean, however, the positive longwave ERFari of all aerosol particles is smaller than the negative shortwave ERFari. As a result, the net aerosol ERFari in GCM estimates is negative (Forster et al., 2021).

To account for particle size (or mass) and chemical composition when estimating ERFari in climate models, extinction is usually defined in terms of an extinction coefficient specific to each aerosol type (eq. 2.8). Here we are interested in the mass extinction coefficient (MEC), which is given in $m^2\,kg^{-1}$.

The median MEC values for different aerosol types from 14 GCMs are $10.3\,m^2\,g^{-1}$ for BC, $8.5\,m^2\,g^{-1}$ for sulfate, $6.1\,m^2\,g^{-1}$ for POA, $5.5\,m^2\,g^{-1}$ for nitrate, $2.8\,m^2\,g^{-1}$ for sea salt aerosols, and $0.74\,m^2\,g^{-1}$ for mineral dust (Gliß et al., 2021, Table 6.2). The MECs for sulfate, nitrate, and carbonaceous aerosols are larger than those for sea salt and mineral dust because of their higher scattering efficiency due to their generally smaller sizes (Figure 6.16). MECs also have a large contribution from accumulation mode particles, because their sizes are comparable to that of the visible light, causing an efficient extinction. The median values of the Mass absorption coefficients (MACs) are $8.5\,m^2\,g^{-1}$ for BC, $0.13\,m^2\,g^{-1}$ for POA, and $0.04\,m^2\,g^{-1}$ for mineral dust (Gliß et al., 2021), indicating that the extinction of solar radiation by BC is dominated by absorption, whereas absorption plays a minor role for all other aerosol types.

https://doi.org/10.1017/9781009485654.013 Published online by Cambridge University Press

The shortwave effect of aerosol particles is often quantified in terms of the aerosol optical depth τ_{AP} . τ_{AP} describes how much solar radiation of a given wavelength becomes extinct by aerosol particles from TOA down to a height z:

$$\frac{I_\lambda(z)}{I_{\lambda,0}} = \exp\left[-\int_z^{\mathrm{TOA}} k_{\lambda,ext} dz\right] = \exp(-\tau_{AP}). \tag{12.1}$$

This equation is a specific version of eq. (2.11), because here the extinction only results from aerosol particles and the radiation path through the atmosphere is in the vertical direction, that is, $ds = dz$.

Here, $I_{\lambda,0}$ is the intensity of radiation at the TOA, and $k_{\lambda,ext}$ is the wavelength-dependent extinction coefficient (eq. 2.9). Both τ_{AP} (eq. 12.1) and the cloud optical depth τ_{cl} (eq. 2.20) are key descriptors for the radiative properties of aerosols and clouds and are often used to quantify their climate impacts.

By definition, τ_{AP} and τ_{cl} are zero at the TOA and increase downward, that is, toward the Earth's surface. If $\tau_{AP} = 1$, the solar radiation is reduced to $1/e = 36.8\,\%$ compared to its values at TOA due to the presence of aerosol particles, and likewise for τ_{cl}.

τ_{AP} aggregates the radiative influence of the various aerosol species into one quantity. Figure 12.3 shows the geographical distribution of the observed annual mean τ_{AP} as obtained from MODIS on board the Terra and Aqua satellites at a wavelength of 550 nm in cloud-free regions. The wavelength 550 nm has been chosen because it lies in the middle of the visible wavelength range ($0.38 \leq \lambda \leq 0.78\,\mu$m). τ_{AP} over land can be retrieved most reliably over dark surfaces with a homogeneous surface albedo, because the reflected radiation from the surface and the extinction by gases need to be subtracted from the reflected radiation in order to isolate the τ_{AP}. Consequently, MODIS cannot retrieve τ_{AP} well over snow and ice and therefore does not include τ_{AP} retrievals over snow and ice-covered surfaces (Li et al., 2005). This explains the lack of data over Greenland and Antarctica in Figure 12.3. Maxima in τ_{AP}

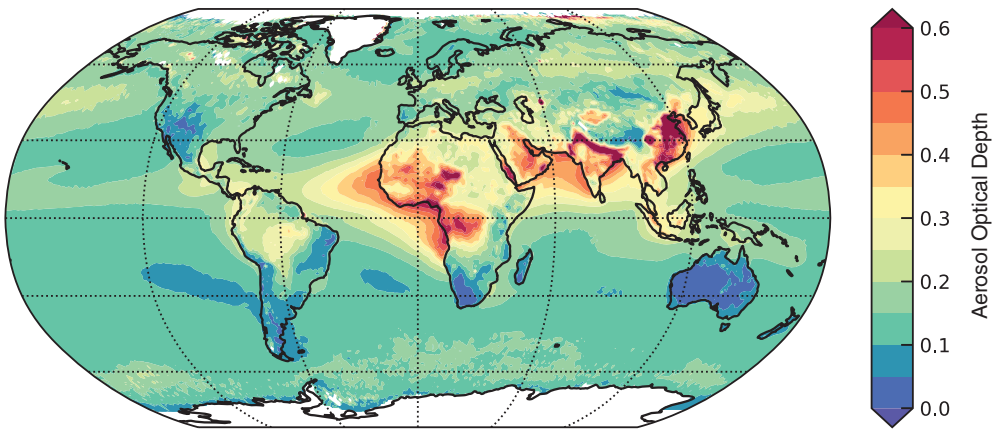


Figure 12.3 Annual mean aerosol optical depth at a wavelength of $\lambda = 550$ nm as determined from the MODIS satellite instrument from March 2000 to December 2023 based on the methods described in Platnick (2015) and Platnick et al. (2017).

https://doi.org/10.1017/9781009485654.013 Published online by Cambridge University Press

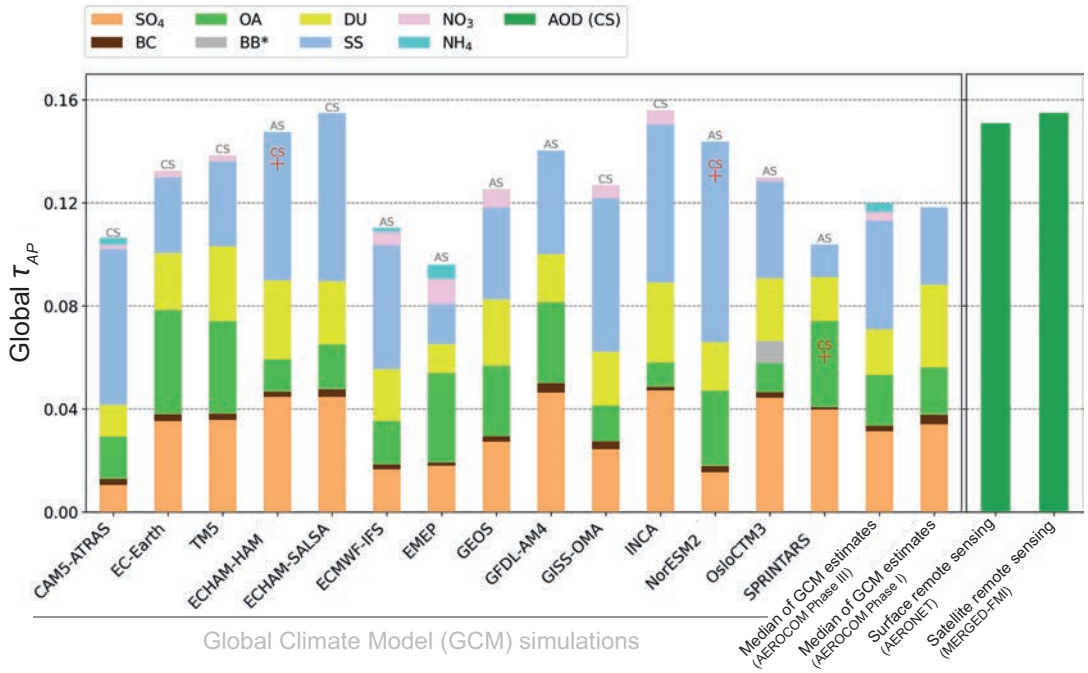


Figure 12.4 Simulated contributions of eight aerosol types, SO_4, BC, OA, biomass burning aerosols (BB), DU, SS, nitrate (NO_3), and ammonium (NH_4) to the global τ_{AP} together with ground-based AERONET observations and the multi-satellite global τ_{AP} product MERGED-FMI for the year 2010. CS denotes τ_{AP} estimates under clear-sky conditions and AS for all-sky conditions. Also depicted are the medians of the global estimates across all models for AEROCOM phase III and phase I. Phase I simulations (Kinne et al., 2006), used data from the year 2000. Figure adapted from Gliß et al. (2021).

are visible downwind of the Sahara Desert, off the west coast of Africa, resulting from desert dust particles and biomass burning particles being transported westwards. Biomass burning also causes high τ_{AP} values over central Africa, the Amazon, and southeast Asia. Fossil fuel combustion adds to the high τ_{AP} values in East Asia and India.

The estimated contribution of different aerosol types to the annual global mean τ_{AP} at a wavelength 550 nm from observations and various GCMs simulations is shown in Figure 12.4 (Gliß et al., 2021). The data in Figure 12.4 are obtained from the AEROCOM phase III and denote observations and simulation data for the year 2010. Here, the annual, global mean τ_{AP} is estimated from both surface remote sensing sites (AERONET in Figure 12.4) and from satellite data (MERGED-FMI in Figure 12.4) to amount to 0.15 in 2010. This is less than the global-mean τ_{AP} of 0.18 obtained from the MODIS satellite data in Figure 12.3 because of the different time periods. The difference also indicates the uncertainty related to τ_{AP} retrievals (Schutgens et al., 2020). While only the total τ_{AP} can be estimated from observations, GCM simulations can be used to estimate the contributions of individual aerosol types based on prescribed radiative properties of these aerosol types and their emission fluxes. Most GCMs include sea salt (SS), mineral dust (DU), POA, BC, and sulfate (SO_4). Their total τ_{AP} is mostly lower than that obtained from observations (Figure 12.4). More strikingly, the contributions

https://doi.org/10.1017/9781009485654.013 Published online by Cambridge University Press

of the different aerosol types differ vastly between the 14 GCMs due to different assumptions within these models.

While mineral dust has the largest aerosol burden (vertically integrated mass mixing ratio), its global contribution to τ_{AP} is only 16 % in the multimodel median (Gliß et al., 2021). Thus, it is comparable to the contribution of organic matter, whose burden is only 12 % of that of mineral dust (Table 6.4). The large contribution of sulfate aerosol particles to τ_{AP} is caused by its high MEC value, which is three and nine times larger than that of sea salt and mineral dust, respectively. The remaining contribution to τ_{AP} originates from POA and BC.

Absorption of solar radiation by BC particles results in a local heating. This diabatic heating may cause cloud droplets to (partly) evaporate, which in turn causes the cloud cover to decrease, allowing more solar radiation to reach and be absorbed in the Earth-atmosphere system (Kaufman and Nakajima, 1993; Ackerman et al., 2000). This adjustment to IRFari, formerly called the aerosol semi-direct effect, can heat the surrounding air, create buoyancy and hence affect cloud formation and the static stability of the atmosphere. Furthermore, cloud droplets can act as lenses for solar radiation and enhance the amount of solar radiation that is absorbed by BC particles inside cloud droplets (Chýlek et al., 1996; Budhavant et al., 2020). The same applies when BC particles are coated with water-soluble material. Because of its high absorption and the associated changes in static stability, the increase in BC due to anthropogenic activity has also been hypothesized to have caused shifts in precipitation patterns in India and China (Menon et al., 2002).

Overall, aerosol particles extinguish (solar) radiation and lead to a net cooling of the Earth's climate. The reduction of solar radiation at the surface by anthropogenic aerosol particles between the 1950s and the 1980s has been termed *global dimming*. With the introduction of clean air legislation in some countries, anthropogenic aerosol emissions have been declining in Europe and North America and the dimming trend has been reversed into a *global brightening* trend between the 1980s and 2000s (Wild, 2012, 2016).

12.1.2 Effective Radiative Forcing due to Aerosol–Cloud Interactions

As discussed in Chapters 7 and 9, aerosol particles can act as CCN and INPs and therefore can affect cloud microphysical and radiative properties, and thus Earth's radiation balance. Yet, the mechanisms of aerosol–cloud interactions remain the most uncertain of all climate forcing agents (Kreidenweis et al., 2019; Bellouin et al., 2020; Forster et al., 2021) and a topic of active research (e.g., Fan et al., 2016). In the following, we provide an overview of the current understanding of aerosol–cloud interactions and the resulting ERF.

An important example of the ERFaci is the instantaneous Twomey effect, shown in Figure 12.5, which might cause several adjustments (Forster et al., 2021). When more aerosol particles are present in the atmosphere (e.g., from anthropogenic pollution), more cloud droplets can form on these particles. If the cloud liquid water content remains constant, an increase in cloud droplets implies that the cloud droplets are smaller. The larger number concentration of smaller cloud droplets increases the total surface area and cross-sectional area of the cloud. As the fraction of reflected solar radiation is proportional to the total cross-sectional area of hydrometeors per projected area of a cloud, a polluted cloud has a higher

https://doi.org/10.1017/9781009485654.013 Published online by Cambridge University Press

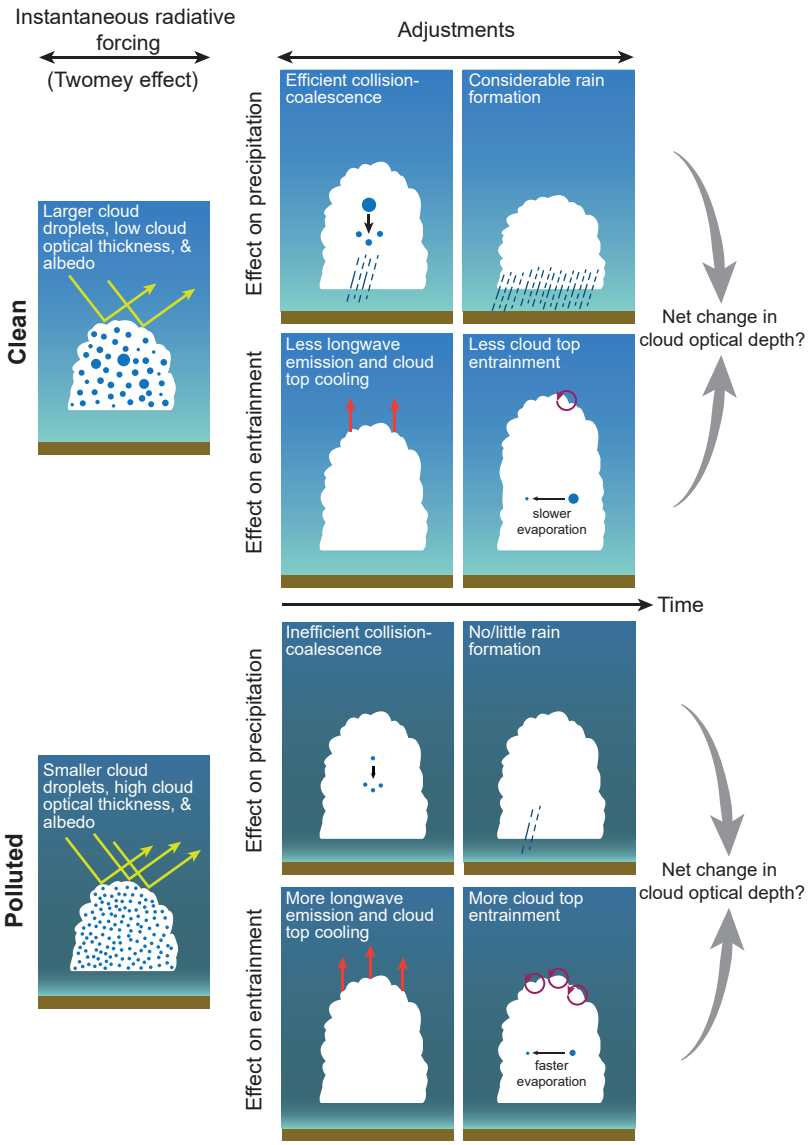


Figure 12.5 Schematic of possible liquid cloud responses to aerosol responses. Whether the entrainment or precipitation response dominates determines the direction of the change in cloud optical depth and the magnitude of ERF due to aerosol–cloud interactions (ERFaci).

cloud albedo compared to a cloud with the same LWC but formed on fewer CCN (Twomey, 1974, 1977; Denman et al., 2007), called the *Twomey effect*. The polluted cloud thus reflects a larger fraction of solar radiation back to space and causes a negative IRF due to aerosol–cloud interactions (IRFaci).

Evidence for IRFaci in liquid clouds can be seen in satellite pictures of so-called *ship tracks* (Figure 1.4f), which are line-shaped clouds that form in the wake of ships (Figure 1.4f). The

https://doi.org/10.1017/9781009485654.013 Published online by Cambridge University Press

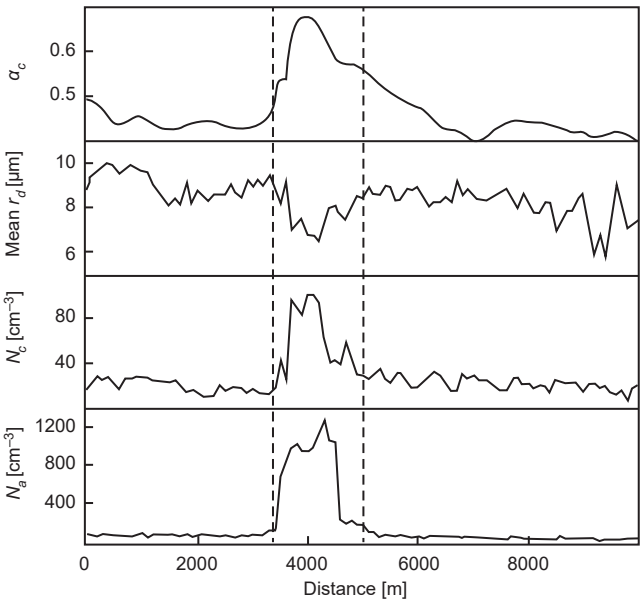


Figure 12.6 Aircraft measurements of cloud albedo α_c, mean cloud droplet radius r_d, cloud droplet number concentration N_c, and accumulation-mode (0.1–1 μm) aerosol number concentrations N_a across a ship track off the coast of California. The ship track is situated between the broken vertical lines. The measurements were taken about 30 min after emission from the ship: the albedo values were obtained from radiation measurements 150 m above the cloud layer, and all other data were obtained from flights 20–50 m below the cloud top. Figure adapted from Durkee et al. (2000). ©American Meteorological Society. Used with permission.

exhaust of ships provides a source of CCN, causing an increase in the cloud droplet number concentration with droplets of smaller sizes and thus ultimately enhances the cloud reflectivity (Coakley Jr. et al., 1987; Radke et al., 1989; Ackerman et al., 2000b). The changes in cloud microphysics in a ship track off the coast of California compared with the adjacent background stratus cloud are shown in Figure 12.6 (Durkee et al., 2000). The figure shows aircraft measurements taken on a flight through a ship track. Within the ship track, indicated by the broken vertical lines, a tenfold increase in the accumulation-mode aerosol concentration was observed. The aerosol increase caused an increase in the cloud droplet number concentration from 20 to 90 cm^{-3} and a decrease in the mean cloud droplet radius by approximately 2 μm. As discussed earlier, a larger concentration of smaller droplets increases the total projected area of the cloud droplets and thus the cloud albedo α_c, in this case from below 0.5 to almost 0.7. This is consistent with laboratory measurements that simulate the Twomey effect in a cloud chamber, as shown in Figure 12.7. For decreasing aerosol concentrations, a decrease in the cloud droplet number concentration and an increase in the mean droplet diameter were observed.

https://doi.org/10.1017/9781009485654.013 Published online by Cambridge University Press

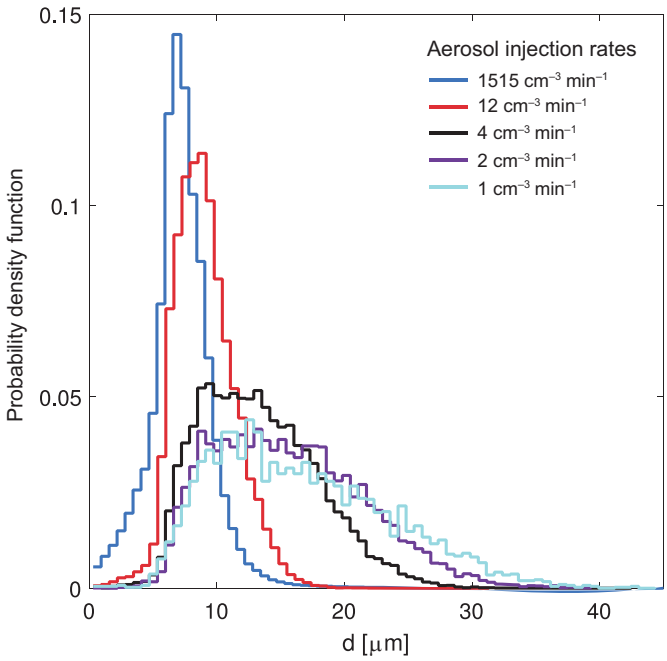


Figure 12.7 Laboratory measurements showing probability density functions of the cloud droplet number size distributions observed in a cloud chamber, for different aerosol injection rates (aerosol loadings, as indicated by the legend). Figure from Chandrakar et al. (2016).

Besides the Twomey effect (i.e., the IRFaci), an increase in aerosol particles may lead to several adjustments in the cloud microphysical properties (Forster et al., 2021). One adjustment that influences warm boundary layer clouds is precipitation suppression (Albrecht, 1989), described as follows and shown in Figure 12.5: In clean, pristine conditions, where only a few CCN are present, a cloud typically has a low cloud droplet number concentration with a rather broad size distribution (e.g., Figure 1.23). Such clouds typically have at least some large droplets, such as the marine cumuli shown in Figure 1.22b. These large droplets initiate the collision–coalescence process (Section 8.2) and readily form drizzle. In contrast, a polluted cloud that forms on more CCN typically has a narrower cloud droplet size distribution, typical of the continental cumuli shown in Figure 1.22c. This narrowing in the droplet size distribution is also visible in the laboratory measurements shown in Figure 12.7 (Chandrakar et al., 2016). It results because more and smaller cloud droplets have to compete for the available water vapor and so grow more slowly. These smaller cloud droplets have a smaller collision efficiency (e.g., Gunn and Phillips, 1957, Section 8.2). Consequently, precipitation formation is often delayed or even suppressed compared to the clean cloud case. Such suppressed drizzle and precipitation formation in polluted clouds has been documented in both observations and numerical model simulations (Ackerman et al., 2003; Wood, 2005). A reduction in drizzle formation is also associated with a smaller wet scavenging rate of aerosol particles, causing them to accumulate in the boundary layer. While the effect of the aerosol number concentration on the cloud droplet size distribution and precipitation formation was already observed in early laboratory studies (e.g., Gunn and Phillips, 1957), it has remained difficult to establish climatological relationships and trends between aerosols, clouds, and precipitation (Stevens and Feingold, 2009).

https://doi.org/10.1017/9781009485654.013 Published online by Cambridge University Press

As it takes longer for precipitation-sized droplets to form in polluted clouds, it has been hypothesized that polluted clouds live longer and hence reflect more solar radiation back to space than clean clouds (Albrecht, 1989). However, a model study that traced individual air parcels having different aerosol number concentrations, from very clean to very polluted, did not find an increase in lifetime for polluted cumulus clouds (Jiang et al., 2006). The polluted cloud has a larger optical depth (e.g., Possner et al., 2017, eq. 2.20 and Section 5.2.6) and emits more longwave radiation than the clean cloud, causing more cloud-top cooling. This cloud-top cooling creates an instability, which creates local convection and due to mass conservation, entrains air from above the cloud into the cloud (Figure 12.5). Depending on the relative humidity above cloud, this entrainment can cause evaporation of cloud droplets. Whether precipitation suppression or evaporation due to entrainment prevails depends on the relative humidity above the boundary layer (Ackerman et al., 2004).

In addition, ship tracks can develop a plume-like structure within cloud-free regions on both sides of the (line-shaped) ship track cloud (Porch et al., 1990). Thus, when their liquid water content and the cloud radiative effect are averaged over the ship tracks, including the adjacent cloud-free regions, even an enhanced liquid water content could be averaged out. Because ship tracks only form in specific environmental conditions (ship exhaust is only visible as a ship track in satellite images less than 1 % of the time), this constitutes a selection bias (Manshausen et al., 2022). For these reasons, using ship tracks to estimate the effects of anthropogenic aerosols on ERFaci globally often results in an overestimation of the IRFaci. On the contrary, during persistent anthropogenic pollution, the enhanced entrainment rate in polluted clouds leads to a new equilibrium state with a lower LWP, that is, a smaller ERFaci, than if the LWP would have remained constant (Glassmeier et al., 2021). In other words, the studies by Ackerman et al. (2004), Jiang et al. (2006), and Glassmeier et al. (2021) call into question if pollution changes the cloud lifetime systematically in one direction.

Differences of ERFaci associated with ship emissions as compared to ERFaci from larger-scale anthropogenic aerosol perturbations have led scientists to focus on larger-scale perturbations of longer duration in so-called *opportunistic experiments* (Christensen et al., 2022) to study ERFaci and use, for example, satellite retrievals to constrain the Twomey effect (Quaas et al., 2020). For instance, Malavelle et al. (2017) analyzed the aerosol perturbation from the 2-months effusive volcanic Holuhraun eruption in Island in 2014. They found an increase in cloud droplet number concentration, a decrease in cloud droplet size, but no change in LWP, thus confirming the IRFaci (Twomey effect). Adjustments caused an increase in total cloud coverage in the MODIS satellite data during the volcanic eruption, a response that current GCMs do not capture (e.g., Malavelle et al. 2017). Instead, the involved GCMs simulated an increase in LWP. In another study, Chen et al. (2022) quantified the ERFaci from the Holuhraun eruption by using machine-learning to disentangle IRFaci from the adjustments and concluded that adjustments in the form of an increase in cloud coverage dominate over the IRFaci, confirming the Malavelle et al. (2017) results.

The Twomey effect was first suggested for liquid clouds by Twomey (1974, 1977), but acts similarly in ice clouds (Kärcher and Lohmann, 2003). Next to changes in CCN number concentration and thus cloud droplet number concentration and size, changes in the INP number concentration can also induce changes in ice nucleation and thus in the frequency of occurrence of glaciation of supercooled clouds or the vertical extent of clouds (Lohmann and Feichter,

https://doi.org/10.1017/9781009485654.013 Published online by Cambridge University Press

2005; Lohmann, 2017; Toll et al., 2024). One example in this context are adjustments that contribute to the ERFaci via changes in mixed-phase clouds. If anthropogenic activity leads to an increase in INPs, this would result in the rapid glaciation of a supercooled liquid cloud through the Wegener–Bergeron–Findeisen process (Figure 3.14). As long as supercooled cloud droplets are present, the cloud is at or above liquid water saturation and hence is supersaturated with respect to ice. Thus, the ice crystals can quickly reach precipitation size and potentially turn a non-precipitating cloud into a precipitating cloud. The glaciation effect was found to lead to a reduction in mixed-phase cloud cover, resulting in a decrease in reflected shortwave radiation, a response opposite to that of adding CCN (Lohmann, 2002*a*).

At the same time, anthropogenic activity leads to an increase in secondary aerosol particles (Table 6.4). If sulfate, nitrate, or organics condense on INPs, such a coating can cover their ice active sites (Section 9.1.5) and thus reduce their INP ability. This so-called deactivation effect causes more clouds to remain supercooled, making precipitation production less efficient, and more shortwave radiation would be reflected to space (Hoose et al., 2008; Storelvmo et al., 2008). As an example, if clouds at temperatures between −35 and 0 °C consisted only of supercooled liquid water, they would reflect 17 W m^{-2} more shortwave radiation back to space, as compared to the same cloud consisting purely of ice (Lohmann, 2002b). Whether the glaciation or the deactivation mechanism dominates, how large they are and to which degree these effects contribute to ERFaci is still a matter of debate (Bellouin et al., 2020).

Another proposed adjustment caused by anthropogenic aerosol particles is invigoration of convective clouds (Koren et al., 2005; Rosenfeld et al., 2008; Varble et al., 2023). The reduced warm-rain formation in the lower part of the convective cloud implies a higher liquid water content, which is thought to release more latent heat of freezing upon lifting. Hence, convection in polluted areas is thought to lead to vertically deeper clouds with longer lifetimes and hence an enhanced shortwave reflectivity, as compared to convective clouds in pristine areas, as illustrated in Figure 12.8 (Lohmann, 2017). This view has been challenged because the enhanced hydrometeor concentration (and slower precipitation formation) implies a higher weight of the total hydrometeors. This in turn exerts a larger gravity force (Section 5.2.6), which instead of an invigoration could lead to a weakening of convective clouds (Igel and van den Heever, 2021; Varble et al., 2023). Igel and van den Heever (2021), nevertheless, confirmed an invigoration of convective clouds, not caused by freezing, but by a mechanism in the liquid phase: The condensation rate in a polluted environment (for the same updraft speed) is larger because of the larger total hydrometeor surface area, which causes an increased latent heat release during condensation of the supersaturated vapor phase on the additional aerosol particles (CCN), ultimately intensifying convection (Fan et al., 2018).

The presence of enhanced aerosol number concentrations can also affect cloud patterns, and hence affect ERFaci (e.g., Rosenfeld et al., 2006; Christensen et al., 2020). For example, Rosenfeld et al. (2006) hypothesized that open cells could transition to the closed-cell cloud pattern by anthropogenic emissions from ships if these perturbations prevent drizzle formation (Figure 1.17). A detailed modelling study by Feingold et al. (2015) supports this hypothesis in cases of large aerosol intrusions that reach the cloud layer before the heaviest drizzle occurs in the early morning hours, and the free troposphere is cloud-free. Such a conversion of an open-cell cloud regime to a closed-cell cloud regime increases the planetary albedo.

https://doi.org/10.1017/9781009485654.013 Published online by Cambridge University Press

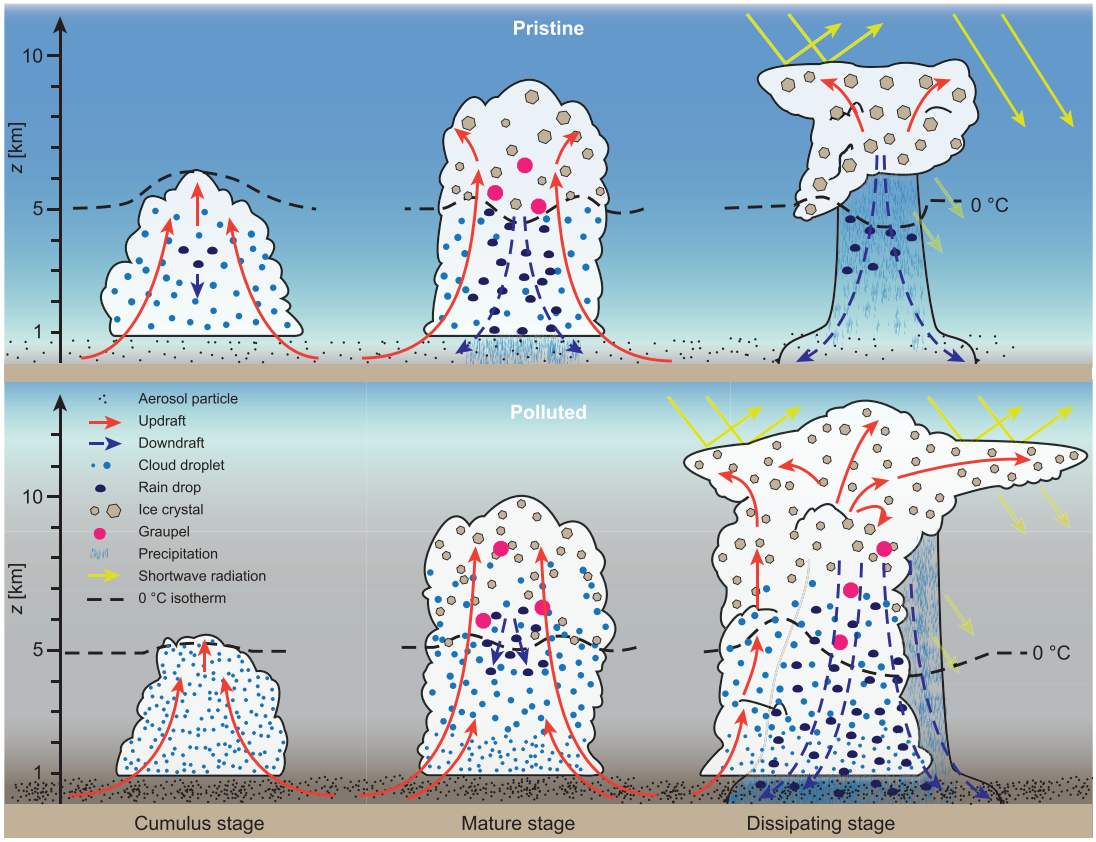


Figure 12.8 Schematic of aerosol-induced convective cloud invigoration by comparing a pristine environment with low aerosol number concentration (top) and a polluted environment with high aerosol number concentration (bottom). Figure adapted from Lohmann (2017).

12.1.3 Comparison of Radiative Forcings

The ERF of the different radiative forcing agents between 1750 (pre-industrial times) and 2019 is summarized in Figure 12.9 (Forster et al., 2021). While annual updates to the state of the climate systems are provided (e.g., Forster et al., 2024), here we discuss the data from AR6. Since 1750, WMGHGs have caused a positive radiative forcing of 3.32 $W\,m^{-2}$. WMGHGs are long-lived GHGs, because their lifetimes of decades to centuries are long enough for these gases to become approximately homogeneously mixed throughout the troposphere (Table 12.1). WMGHGs include carbon dioxide (CO_2), methane (CH_4), nitrous oxide (N_2O), and halogens. CO_2 is the main contributor to the ERF of these WMGHGs with 2.16 (1.9 to 2.41) $W\,m^{-2}$, corresponding to an increase in concentration from 278.3 ppm to 410.5 ± 0.2 ppm in 2019[2] (Table 12.1). The second-largest WMGHG is CH_4 with an ERF of 0.54 (0.43 to 0.65) $W\,m^{-2}$, corresponding to an increase in concentration from 729.2 ppb to 1877 ± 2 ppb in

[2] https://public.wmo.int/en/greenhouse-gas-bulletin-no-19

https://doi.org/10.1017/9781009485654.013 Published online by Cambridge University Press

Table 12.1 Greenhouse gas concentrations obtained from WMO, given in volume mixing ratios for pre-industrial conditions, for 2019 for comparibility with IPCC AR6, and for 2022. Also tabulated are atmospheric lifetimes, taken from Canadell et al. (2021) for CH_4 and N_2O and from Ciais et al. (2013) for CO_2. The lifetime of CO_2 depends on from which sink process (land uptake, ocean invasion, reaction with $CaCO_3$, or silicate weathering) it is calculated.

GHG	1750 (pre-industrial)	2019 (present-day)	2022 (present-day)	Lifetime
CO_2	278.3 ppm	410.5 ± 0.2 ppm	417.9 ± 0.2 ppm	1 yr to 10^6 yr
CH_4	729.2 ppb	1877 ± 2 ppb	1923 ± 2 ppb	9.1 yr
N_2O	270.1 ppb	332.0 ± 0.1 ppb	335.8 ± 0.1 ppb	116 yr

2019 (Table 12.1). Moreover, Figure 12.9 shows that halocarbons, hydrocarbons where at least one carbon atom is covalently linked to a halogen atom (fluorine, chlorine, bromine, or iodine), have an ERF of 0.41 (0.33 to 0.49) $W\,m^{-2}$ and N_2O has an ERF of 0.21 (0.18 to 0.24) $W\,m^{-2}$. The latter corresponds to an increase in concentration from 270.1 ppb to 332.0 ± 0.1 ppb in 2019 (Table 12.1). The ERF numbers indicated in brackets in Figure 12.9 denote the 5–95 % confidence interval.

Due to the homogeneous distribution of WMGHGs throughout the troposphere, only a few observational sites are necessary to reliably measure their concentration. Therefore, the behavior and changes of WMGHGs are well understood, and the ERF of WMGHGs is associated with a rather small 5–95 % uncertainty range compared to that of the other forcing agents.

For ozone, the ERF has two contributions, one from stratospheric ozone and one from tropospheric ozone. Stratospheric ozone (the ozone layer) absorbs most of the Sun's incoming ultraviolet radiation. Decreases in stratospheric ozone that historically have been caused by halogen-containing substances, which are banned since the Montreal protocol in 1998, lead to less absorbed ultraviolet radiation, causing a smaller ERF by ozone (e.g., Stähelin et al., 2001; Ball et al., 2018).

Tropospheric ozone is an example of a non-WMGHG, because of its short lifetime. It causes an increasingly positive ERF because it has increased from pre-industrial times to the present day. It is formed mainly during summer by the photo-chemical oxidation of its precursor gases (nitrogen oxides, carbon monoxide, and volatile organic compounds), which have been increasing since pre-industrial times.

In total, the combined ERF of stratospheric and tropospheric ozone amounts to 0.47 (0.24 to 0.71) $W\,m^{-2}$ (Figure 12.9, Forster et al., 2021).

In the stratosphere, water vapor is produced by the oxidation of methane with the hydroxyl radical (Frank et al., 2018). Its stratospheric lifetime is on the order of years, resulting in a small positive ERF of 0.05 (0.0 to 0.1) $W\,m^{-2}$.

Notably, aerosol particles are associated with the largest negative ERF but also with a large uncertainty range (Figure 12.9). Anthropogenic aerosol particles cause changes both in ERFari and ERFaci. ERFaci with -0.84 (-1.45 to -0.25) $W\,m^{-2}$ dominates over ERFari of -0.22 (-0.47 to 0.04) $W\,m^{-2}$. Szopa et al. (2021) estimated the individual contributions of

https://doi.org/10.1017/9781009485654.013 Published online by Cambridge University Press

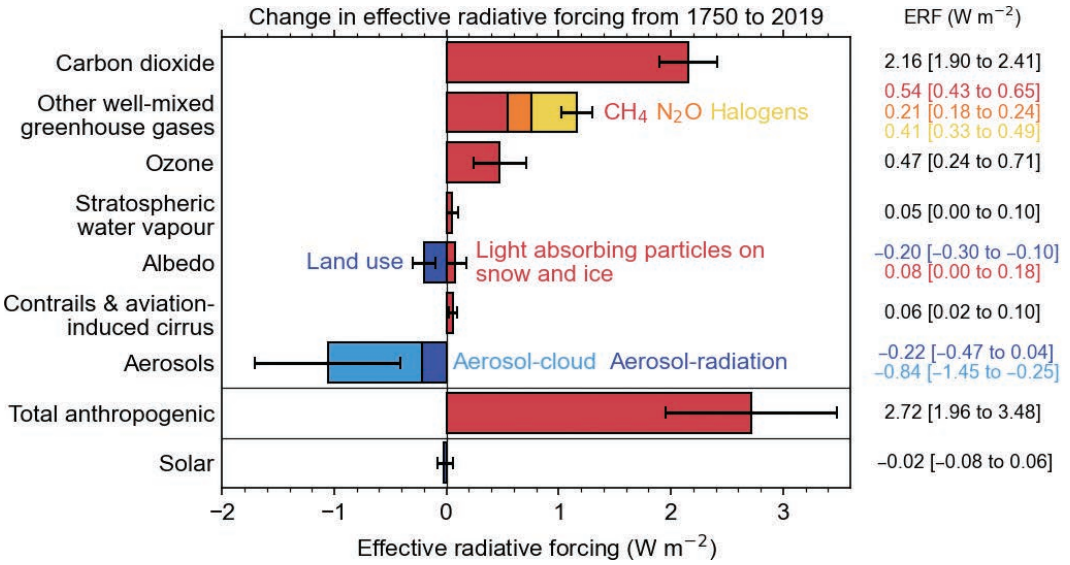


Figure 12.9 Changes in effective radiative forcing estimates in 2019 relative to 1750, along with uncertainties, for the different forcing agents. Solid bars represent the best estimates of the ERFs, with 5–95 % uncertainty intervals shown as error bars. The corresponding values of best estimates and uncertainties are also shown on the right-hand side. Volcanic forcing is not included as its episodic nature makes it difficult to compare with other forcing mechanisms. Figure reproduced from Figure 7.6 of IPCC AR6 (Forster et al., 2021).

different aerosol species and their precursors to ERFari and ERFaci: SO_2 was found to be the largest contributor with a total ERF of -0.94 (-1.63 to -0.25) W m^{-2}, with -0.23 W m^{-2} from ERFari and -0.70 W m^{-2} from ERFaci. Emissions of organic carbon lead to a weaker negative ERF of -0.21 (-0.44 to 0.02) W m^{-2}. This has two main reasons: First, their lower hygroscopicity factor κ (Table 7.3) implies that they are not as large as sulfate or sea salt aerosols at high relative humidities, and therefore do not activate to cloud droplets as readily. Hence, they have a smaller ERFaci than sulfate aerosols. Secondly, in the form of brown carbon, they absorb some solar radiation and therefore scatter less solar radiation back to space, resulting in a weaker negative ERFari than that of SO_2 (Chung et al., 2012). By contrast, the net ERF of BC is slightly positive with 0.11 (-0.2 to 0.42) W m^{-2}. While BC aerosols strongly absorb solar radiation and therefore have a positive ERFari, their ERFaci is less well understood (e.g., Bond et al., 2013). This is also reflected in the uncertainty range of the ERF of BC, ranging from a net negative to a net positive value. Whether the ERFaci of BC contributes to a warming or cooling depends on (among others) the cloud type affected by BC. For instance, BC particles can act as CCN if they are internally mixed with soluble/hygroscopic aerosols or become sufficiently hydrophilic after atmospheric aging by gas-phase oxidants (Friebel et al., 2019).

Such an increased CCN activity of BC increases the reflectivity of low clouds, leading to a negative ERFaci. Soot particles may act as INPs, depending on their size, the soot type, and their degree of atmospheric aging (Testa et al., 2024). Soot particles that promote heterogeneous ice nucleation can increase the optical thickness of high clouds, which leads to a positive ERFaci (Lohmann et al., 2020).

https://doi.org/10.1017/9781009485654.013 Published online by Cambridge University Press

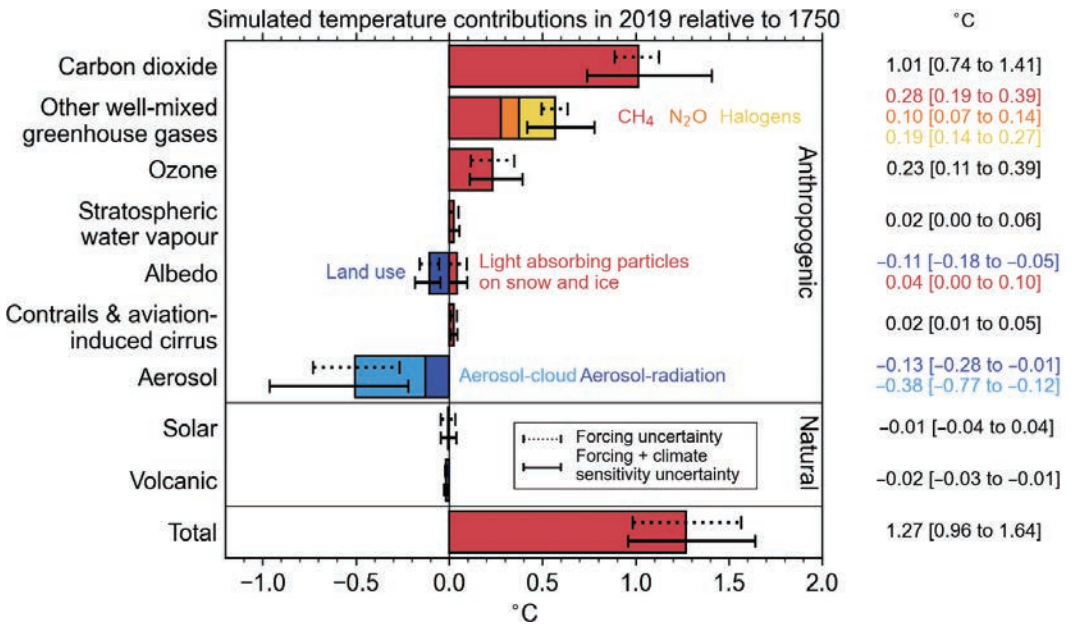


Figure 12.10 Simulated contributions of the different forcing agents to the 2019 global mean surface air temperature change relative to 1750, along with uncertainties. Solid bars represent the best estimates, with 5–95 % uncertainty intervals shown as error bars. The corresponding values of best estimates and uncertainties are also shown on the right-hand side. Figure reproduced from Figure 7.7 of IPCC AR6 (Forster et al., 2021).

For any forcing agent, the ERF can be converted into surface air temperature contributions with simplied ensemble simulation, termed emulator Monte Carlo simulations as shown in Figure 12.10 (Forster et al., 2021). As a rule of thumb, the changes in surface air temperature are roughly half as large as the ERF changes, with an overall surface air temperature warming of 1.27 (0.96 to 1.64) K compared to the net anthropogenic forcing of 2.72 (1.96 to 3.48) $W\,m^{-2}$. This net warming is dominated by the positive contributions from WMGHGs and ozone of 1.81 K and partly offset by the cooling due to aerosols and land use change of −0.62 K.

12.2 Observed Trends in Total Cloud Cover

While reliable observations of temperature reach back into the 18th century, reliable observations of cloud cover obtained from surface observations only date back to the 1950s. The Extended Cloud Report Archive (Hahn and Warren, 2009; Eastman et al., 2011; Eastman and Warren, 2013) contains cloud observations from ships since 1954 and from land stations since 1971. While other cloud observations, especially over land, predate this archive, data were recorded differently, and the cloud type classification was done differently. Hence, they are not considered here.

The cloud trends from surface observations are shown in Figure 12.11. The total cloud cover over land decreased by 4 % per century between 1971 and 2009, whereas cloud cover

https://doi.org/10.1017/9781009485654.013 Published online by Cambridge University Press

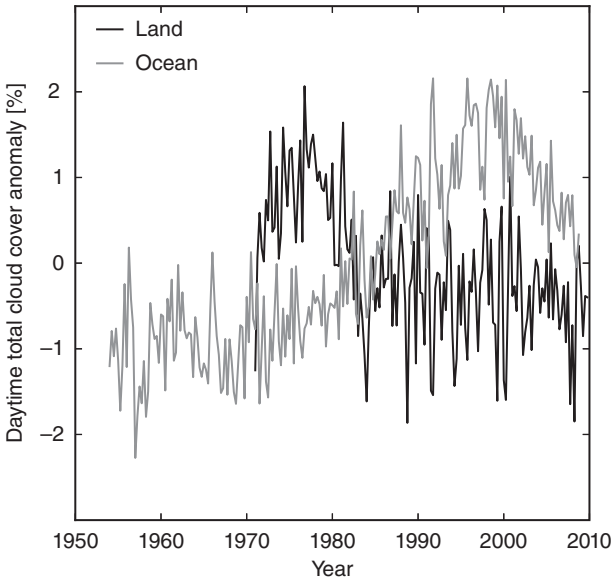


Figure 12.11 Time series of global cloud cover anomalies over land and ocean as obtained from surface observations. Both time series are based on averages of seasonal anomalies from the long-term mean, allocated to individual 10° grid boxes weighted by land or ocean area and relative box size. Figure adapted from Eastman and Warren (2013). ©American Meteorological Society. Used with permission.

over ocean increased by ≈ 4 % (Eastman and Warren, 2013). The decreasing trend over land is caused by decreases in all stratiform clouds (stratus, nimbostratus, altostratus, and cirrus), but the convective cloud types (cumulus, stratocumulus, and altocumulus) showed slight increases over this period. This is consistent with the decrease in stratiform and the increase in convective precipitation, respectively, observed over the past 50 years in Northern Eurasia (Chernokulsky et al., 2019) (Section 10.6).

The increase in cloud cover over the ocean, as obtained from surface observations, contradicts satellite-derived cloud cover trends (Wylie et al., 2005; Tselioudis et al., 2024), which show a decrease in total cloud cover. Therefore, total cloud cover trends have to be interpreted with caution. Ground-based observations of total cloud cover are generally biased toward low clouds because they may obscure mid-level and high clouds. Satellite-based observations, on the contrary, are most sensitive to high clouds (e.g., Protat et al., 2014). These different sensitivities explain at least partly the contrary cloud cover trends over the oceans.

The ocean data in Figure 12.11 have been separated into the different cloud families (low, mid-level, high) by Eastman et al. (2011) as shown in Figure 12.12. It can be seen that the increase in total cloud cover toward the end of the 20th century results from increases in low and high clouds, while the mid-level cloud coverage fluctuates over the analyzed time period 1954–2008. This is related to interannual variability, such as the El Niño/Southern Oscillation circulation. While marine stratus and stratocumulus clouds decrease with increasing SST,

https://doi.org/10.1017/9781009485654.013 Published online by Cambridge University Press

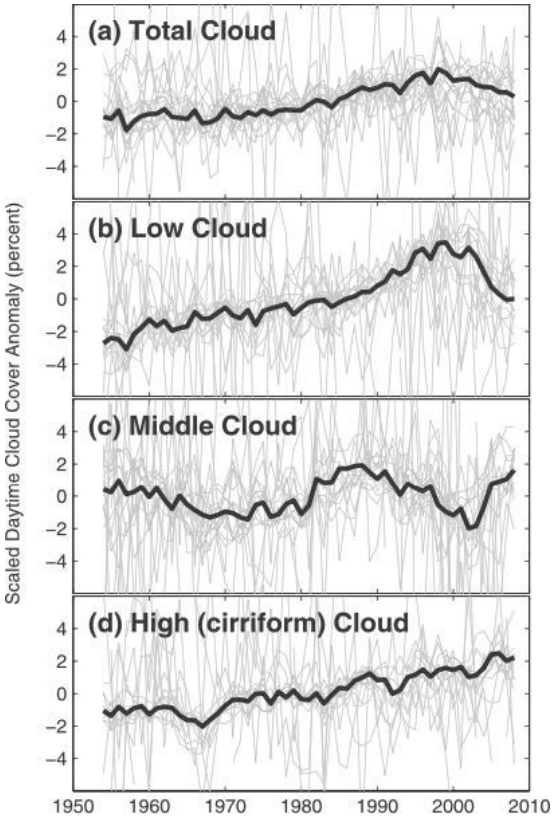


Figure 12.12 Time series of daytime cloud cover anomalies over the ocean from surface observations between 1954 and 2008 for (a) total cloud cover, (b) low clouds, (c) mid-level clouds, and (d) high clouds. Figure adapted from Eastman et al. (2011). ©American Meteorological Society. Used with permission.

cumulus clouds increase. This increase arises because the static stability of the atmosphere decreases with increasing SST (Klein and Hartmann, 1993).

12.3 Climate Feedbacks at the Time of a Doubling of CO_2

After having considered forcing agents and the associated (effective) RF, we will now discuss how the climate system responds to a given RF. If the Earth-atmosphere system is perturbed by an IRF, ΔF, for instance, a doubling of the CO_2 concentration, the radiation balance at the TOA will be affected as follows:

$$\Delta F = \Delta R + \Delta H + \lambda \Delta T_s. \tag{12.2}$$

Here ΔR represents the net radiative imbalance at the TOA, ΔH is the heat taken up by the ocean, ΔT_s is the change in global mean surface temperature, and λ is the climate sensitivity parameter. The climate sensitivity parameter controls the long-term response in T_s for a given forcing. This is illustrated in Figure 12.1 where depending on the climate sensitivity parameter, the new equilibrium (T_s) is given by the empty or filled green circle.

https://doi.org/10.1017/9781009485654.013 Published online by Cambridge University Press

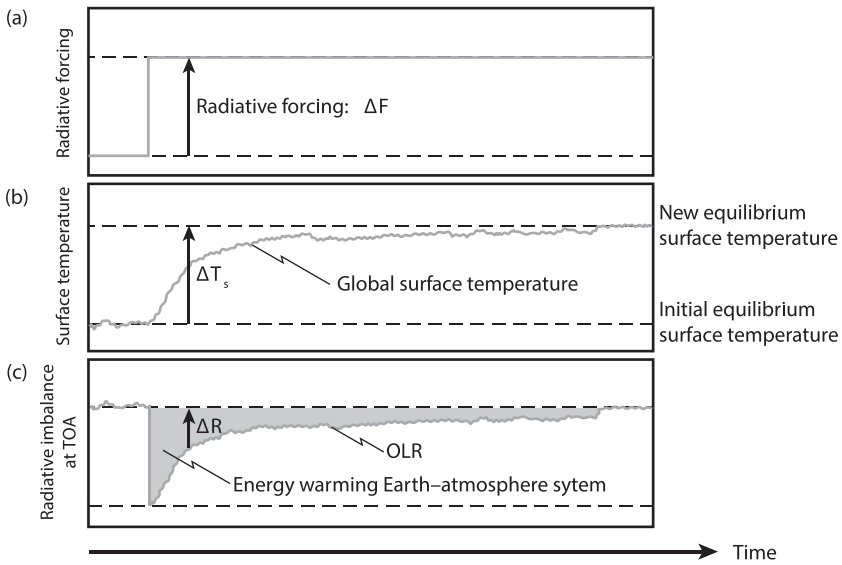


Figure 12.13 (a) Schematic of an instantaneous radiative forcing ΔF, (b) response of the Earth-atmosphere system in terms of the global mean surface temperature T_s, and (c) the net radiative imbalance ΔR and Outgoing longwave radiation (OLR). Figure adapted from Murphy et al. (2009).

The quantities in eq. (12.2) change over time except for ΔF, which in our example is caused by a step change from $1 \times CO_2$ to $2 \times CO_2$, as depicted in Figure 12.13a. After this step change to $2 \times CO_2$, the radiation at the TOA is no longer balanced, as shown in Figure 12.13c, where the Outgoing longwave radiation (OLR) at TOA decreases step-wise at the same time as CO_2 doubles. Initially, this imbalance ΔR equals ΔF. If ΔF and thus ΔR are positive, then over time the land and ocean will warm. According to the Stefan–Boltzmann law (eq. 2.3), the land and the ocean will emit more radiation in response to their higher temperatures. In the new equilibrium, land and ocean emit as much longwave radiation as needed to balance ΔF at the TOA. Hence, the radiative imbalance ΔR at the TOA will be zero once the new equilibrium is reached (Figure 12.13c, corresponding to the green circles in Figure 12.1). Also, the ocean does not take up any more heat at this point, and therefore, $\Delta H = 0$ in the new equilibrium. Consequently, once the new equilibrium is reached, eq. (12.2) reduces to

$$\Delta F = \lambda \Delta T_s. \tag{12.3}$$

12.3.1 Planck feedback

The effective radiative forcing ΔF for $2 \times CO_2$ from its value in 1750 of 278.3 ppm was assessed in IPCC AR6 to be $3.93 \pm 0.47\ \mathrm{W\,m^{-2}}$ (Forster et al., 2021).

https://doi.org/10.1017/9781009485654.013 Published online by Cambridge University Press

Splitting ΔF in eq. (12.3) into its longwave (LW) and shortwave (SW) components yields

$$\lambda = \frac{\Delta F_{LW} - \Delta F_{SW}}{\Delta T_s}. \tag{12.4}$$

Without any climate feedbacks that affect T_s, the change in F_{LW} due to $2 \times CO_2$ in the new equilibrium with $\Delta R = \Delta H = 0$ is given by the derivative of the Stefan–Boltzmann law (eq. 2.3) with respect to the surface temperature:

$$\frac{\Delta F_{LW}}{\Delta T_s} \approx \frac{dF_{LW}}{dT_s} = 4\epsilon\sigma T_s^3 = \frac{4F_{LW}}{T_s}. \tag{12.5}$$

The value of the climate sensitivity parameter calculated using eq. (12.5) is called the *Planck feedback* because the changes in T_s are entirely described by the Stefan–Boltzmann law, which is the Planck function integrated over all wavelengths (Section 2.1.2). Note that this calculation ignores Earth's atmosphere because it calculates dF_{LW}/dT_s from $4\epsilon\sigma T_s^3$. Doing this results in a Planck climate sensitivity parameter λ_{Pl}, given by:

$$\lambda_{Pl} = \frac{\Delta F_{LW}}{\Delta T_s} = \frac{4F_{LW}}{T_s} = \frac{4 \times 398\,\mathrm{W\,m^{-2}}}{289.5\,\mathrm{K}} = 5.5\,\mathrm{W\,m^{-2}\,K^{-1}}, \tag{12.6}$$

where the numbers at the surface have been taken from Figure 2.4. However, this value is too high because not $398\,\mathrm{W\,m^{-2}}$, but only $239\,\mathrm{W\,m^{-2}}$ are emitted to space (Figure 2.4). Therefore, the Planck feedback needs to be estimated from model simulations (e.g., Dufresne and Bony, 2008; Ceppi et al., 2017). Using the multimodel GCM estimate of $\lambda_{Pl} = 3.22\,\mathrm{W\,m^{-2}\,K^{-1}}$ within a very likely range of 3.0 to 3.4 $\mathrm{W\,m^{-2}\,K^{-1}}$ (Forster et al., 2021), and rearranging eq. (12.3) yields

$$\Delta T_s = \frac{\Delta F}{\lambda_{Pl}} = \frac{3.93\,\mathrm{W\,m^{-2}}}{3.22\,\mathrm{W\,m^{-2}\,K^{-1}}} = 1.22\,\mathrm{K}. \tag{12.7}$$

To put it differently, a simple doubling of CO_2 leads to an increase in surface temperature of 1.2 K assuming a (Planck) climate sensitivity of $3.22\,\mathrm{W\,m^{-2}\,K^{-1}}$ (Figure 12.14).

12.3.2 Water Vapor, Lapse Rate, and Surface-Albedo Feedback

In addition to this Planck feedback, several other climate feedbacks occur in response to an increase in T_s (eq. 12.7), as shown in Figure 12.14. Therefore, these additional feedbacks are often referred to as *temperature feedbacks*. As T_s increases, the saturation water vapor pressure increases according to the Clausius–Clapeyron equation (3.70). The relative humidity has been found to remain more or less constant when the lower tropospheric temperature changes (Soden et al., 2002). This implies that the specific humidity increases in a warmer climate. Because water vapor itself is a greenhouse gas, this feedback is positive. More water vapor at higher temperatures implies that the vertical temperature gradient from the Earth's surface to the upper troposphere is reduced. This is because the saturated adiabatic lapse rate is smaller for higher temperatures than for lower temperatures (eq. 4.38). In other words, because convection is more vigorous in a warmer climate and convection moistens and warms the mid-troposphere due to latent heat release, the vertical temperature gradient, that is, the lapse rate,

https://doi.org/10.1017/9781009485654.013 Published online by Cambridge University Press

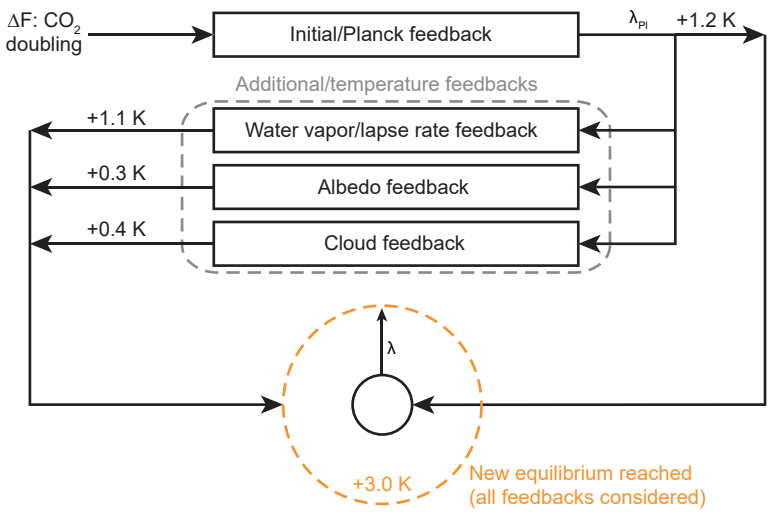


Figure 12.14 Components of the feedbacks associated with a doubling of CO_2, and the respective temperature changes required to reach a new equilibrium, illustrated by the solid and dashed circles. The numbers are taken from Forster et al. (2021).

is smaller in a warmer climate. Since the emission of longwave radiation to space predominantly originates from the mid-troposphere (Section 2.2.2), a warmer troposphere implies that more longwave radiation is emitted to space, corresponding to a negative feedback. Since both the positive water vapor feedback and the negative lapse-rate feedback are linked to water vapor, they are often considered together. The combined water vapor and lapse rate feedback has been assessed in IPCC AR6 to amount to a net warming effect (dominance of water vapor over lapse rate feedback) of $1.3\,W\,m^{-2}\,K^{-1}$ with a very likely range of $(1.1\text{ to }1.5)\,W\,m^{-2}\,K^{-1}$ (Forster et al., 2021), corresponding to a global mean near-surface temperature increase of 1.1 K for a doubling of CO_2.

An increase in T_s leads to the melting of snow and ice surfaces. Melting causes bright surfaces to be replaced by darker surfaces, which absorb more solar radiation (Table 2.1). Unlike the Planck feedback and the combined water vapor and lapse rate feedback, this positive surface-albedo feedback is not of global extent but is spatially limited to areas currently covered by snow and ice (polar and mountainous regions), where it contributes to the amplified temperature increase (e.g., Goosse et al., 2018). The surface-albedo feedback has been assessed in IPCC AR6 to amount to $0.35\,W\,m^{-2}\,K^{-1}$ with a very likely range of $0.1–0.6\,W\,m^{-2}\,K^{-1}$, which corresponds to a global mean near surface temperature increase of 0.3 K for a doubling of CO_2 (Forster et al., 2021).

12.3.3 Cloud Feedbacks

Of the feedbacks shown in Figure 12.14, the cloud feedback has the largest spread between different GCMs and remains the most uncertain feedback (Vial et al., 2013; Boucher et al., 2013; Zelinka et al., 2017). The reasons for this spread and uncertainty are twofold: (i) In a warmer climate, clouds may form at higher altitudes and may have different water contents, phases, and microphysical properties, but the exact nature of this is still unknown. (ii) Because clouds can be smaller than the grid box of a GCM, cloud formation and evolution need to

https://doi.org/10.1017/9781009485654.013 Published online by Cambridge University Press

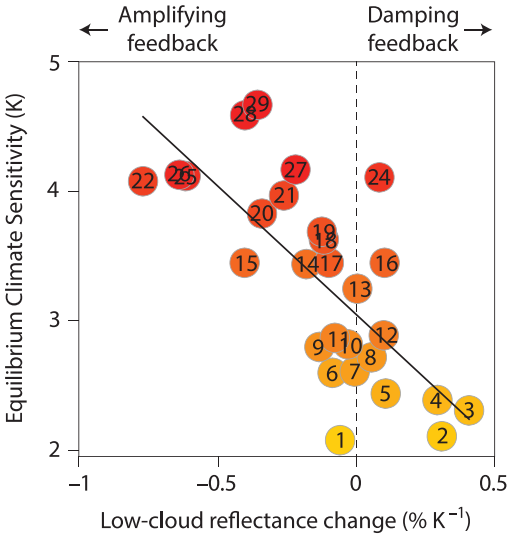


Figure 12.15 Equilibrium climate sensitivity (ECS) versus changes in the amount of sunlight reflected by low clouds over tropical oceans from simulations of 29 different GCMs (colored, numbered circles). Figure adapted from Schneider et al. (2017).

be parameterized, that is, described in terms of large-scale (grid mean) variables. Therefore, GCM simulations have biases when simulating certain cloud types and cloud microphysical properties, inducing uncertainties in climate projections (e.g., Tan et al., 2016; Schneider et al., 2019).

This large uncertainty contributes to the considerable spread in the estimated increase of the equilibrium global mean T_s needed to reach a new equilibrium in response to a doubling of CO_2, the so-called *equilibrium climate sensitivity* (ECS) (e.g., Knutti et al., 2002; Knutti and Hegerl, 2008): for 2 × CO_2, ECS amounts to 3 K and is likely within the range of 2.5–4 K (Forster et al., 2021).

Low clouds

The importance of the changes in tropical low clouds for ECS is highlighted in Figure 12.15, which shows simulation results of 29 different GCMs (Schneider et al., 2017). The temperature increase predicted by the individual GCMs ranges between 2.1 and 4.7 K. There is a clear negative correlation with a linear correlation coefficient $r = 0.73$ between the change in the albedo of tropical low clouds and ECS. Specifically, an increase in the tropical low cloud albedo causes a negative low-cloud feedback in these regions and hence only a moderate ECS. On the contrary, in those GCMs where the reflectance of tropical low clouds decreases, the low cloud feedback is positive and hence leads to an amplification of the warming. All in all, the inter-model differences in cloud feedback give rise to one of the largest uncertainties for estimating the increase in global mean surface temperature (Sherwood et al., 2014; Forster et al., 2021; Vogel et al., 2022).

A positive low cloud feedback for increasing SST can be inferred from Section 12.2, because in four of the six regions investigated by Eastman et al. (2011), the coverage of stratus and stratocumulus clouds decreased more than the amount of cumulus clouds increased. This tendency has also been found from high-resolution simulations (Klein et al., 2017; Schneider et al., 2019;

https://doi.org/10.1017/9781009485654.013 Published online by Cambridge University Press

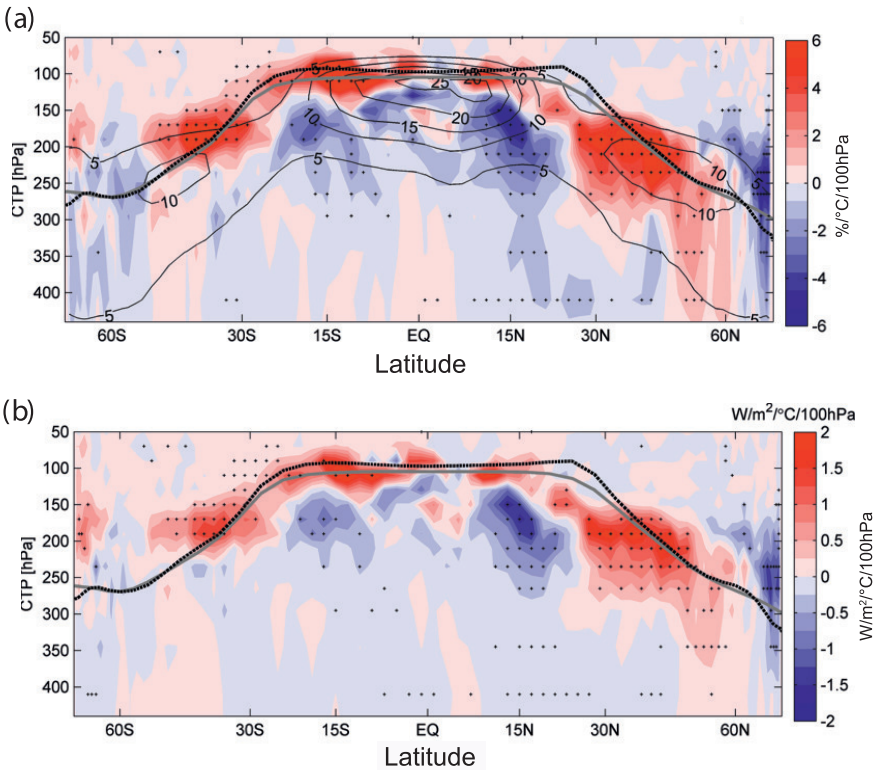


Figure 12.16 (a) Zonal mean response as a function of latitude and Cloud top pressure (CTP) of the cirrus cloud fraction to inter-annual surface warming, calculated by regressing the monthly mean anomalies of cloud fraction from the CALIPSO satellite data against the monthly mean anomalies of global mean surface temperature (ECMWF reanalysis product (ERA-Interim)). The thin black contour lines give the six-year mean cirrus cloud fraction in %, and the gray line denotes the ERA-Interim climatological tropopause pressure. The bold dotted line is the climatological tropopause pressure in response to 1 K surface warming. (b) Cirrus feedback in $W\,m^{-2}\,K^{-1}$ per 100 hPa. The dots denote pixels where the linear regression slope is statistically distinguishable from zero. Figure adapted from Zhou et al. (2014) with permission from the American Geophysical Union.

Sherwood et al., 2020). In conclusion, these findings suggest that GCMs that predict decreasing low clouds in response to a CO_2 doubling (such as in the upper left corner in Figure 12.15) agree better with observations.

High clouds

The change in cirrus cloud coverage (fraction) with increasing temperature is shown in Figure 12.16a. Figure 12.16a indicates that cirrus clouds will shift to higher altitudes in response to a global surface warming. This can most clearly be seen in the tropics (30 °N – 30 °S) where the cirrus cloud fraction generally decreases between 250 and 130 hPa (blue shading) and increases above these altitudes (red shading). This change in cirrus cloud fraction amounts

https://doi.org/10.1017/9781009485654.013 Published online by Cambridge University Press

to up to $6\,\%\,K^{-1}$ per 100 hPa. The midlatitudes of both hemispheres are characterized by an increase in cirrus cloud fraction within the upper troposphere for an increasing surface temperature. From this fractional change in cirrus cloud coverage, the cirrus cloud feedback has been estimated and is shown in Figure 12.16b. A positive cloud feedback (red shading in Figure 12.16b) can be seen in areas where the cirrus cloud cover increases in Figure 12.16a and where the occurrence of cirrus clouds was shifted to higher altitudes. In a given climate, the higher the cirrus clouds, the lower their cloud top temperatures and, according to the Stefan–Boltzmann law (eq. 2.3), the less longwave radiation can be emitted to space. Thus, the LCRE (Section 2.3) of these clouds increases. By contrast, the cirrus cloud feedback is negative at lower altitudes (blue shading in Figure 12.16b), where the cirrus cloud cover decreases in Figure 12.16a. In the global annual mean, the cirrus cloud feedback is net positive, at 0.22 ± 0.12 $W\,m^{-2}\,K^{-1}$ (Zhou et al., 2014; Zelinka et al., 2020; Forster et al., 2021), amounting to half of the overall cloud feedback in Figure 12.14.

General trends and aspects

A summary of the diverse cloud responses to greenhouse gas warming is shown in Figure 12.17 (Forster et al., 2021). The responses are divided into the changes in the thermodynamic structure of the atmosphere that are relevant for cloud formation and the associated changes in clouds themselves. Robust cloud responses to the WMGHG warming are defined as those responses that have been simulated by most GCMs and possess some kind of independent support or physical understanding.

In a warmer climate, the troposphere is expanding in response to the warming of Earth's surface (e.g., Meng et al., 2021). The cloud-top temperature of deep convective clouds in the tropics has been found to remain constant, which is referred to as the *fixed anvil temperature mechanism* (Hartmann and Larson, 2002; Forster et al., 2021). With a fixed anvil temperature and rising Earth's surface temperatures, the depth of the troposphere increases. A deeper tropopause implies a rising of high clouds, because cirrus temperatures are now limited to higher altitudes. Deep convective clouds can also become deeper (increased vertical extent). Both mechanisms are indicated in Figure 12.17. Because the anvil temperature remains the same in a warmer climate, the temperature difference between the anvil and the Earth's surface increases, which in turn increases the LCRE (Section 2.3). Then, the amount of energy emitted to space decreases, leading to a positive cloud feedback. This positive cloud feedback may be partly offset by a reduction in the amount of anvil clouds of -0.15 ± 0.20 $W\,m^{-2}\,K^{-1}$. However, this reduction has only been assessed with low confidence (Forster et al., 2021).

The warmer SSTs cause a decrease in atmospheric stability (Chapter 4). At the same time, the mid-troposphere becomes warmer, increasing the inversion strength (Figure 12.17 and Klein et al., 2017). Overall, changes in cloud types from stratus forming under stable atmospheric conditions to stratocumulus forming under less stable conditions, as well as from stratocumulus to more cumulus clouds, have been observed/associated with climate change (Eastman et al., 2011; Schneider et al., 2019). As the more convective cloud types cover a smaller horizontal area, the cloud coverage of low clouds decreases, indicated as fewer low clouds in Figure 12.17. Overall, this positive cloud feedback of subtropical marine low

https://doi.org/10.1017/9781009485654.013 Published online by Cambridge University Press

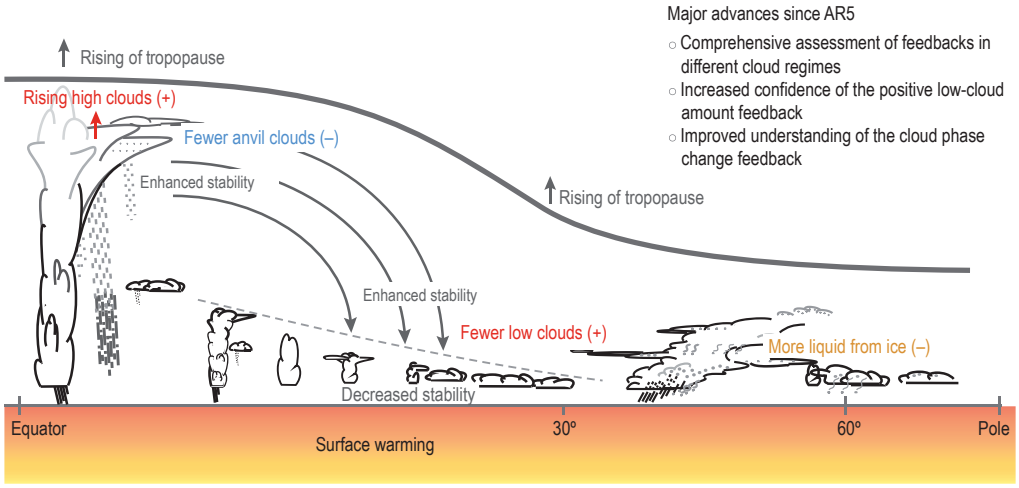


Figure 12.17 Schematic of cloud responses to a surface warming (warming climate). The tropopause is shown by the thick solid line and the subtropical inversion layer by the dashed gray line. Changes in the thermodynamic structure that are relevant to clouds are shown in gray arrows and gray text. The major cloud changes anticipated in a warmer climate shown in red, orange, and blue indicate major cloud responses assessed with high, medium, and low confidence, respectively. The signs of their feedbacks to the surface warming are indicated in the parentheses, and the major advances since IPCC AR5 are listed in the box. Figure adapted from Figure 7.9 of IPCC AR6 (Forster et al., 2021).

clouds equatorward of 30° has been assessed to be $0.20 \pm 0.16\ \mathrm{W\,m^{-2}\,K^{-1}}$ (Forster et al., 2021). In addition, many land areas experience drying, which is propagated to the atmosphere and reduces cloudiness over land, consistent with observations (Figure 12.11). The associated response of low clouds has been assessed to be $0.08 \pm 0.08\ \mathrm{W\,m^{-2}\,K^{-1}}$ with low confidence (Forster et al., 2021).

Observations since 1980 show a widening of the Hadley cell (Gulev et al., 2021), implying a poleward shift of high clouds (Tselioudis et al., 2016). In addition, the storm tracks migrate polewards causing free tropospheric (mid-level and high) clouds to also shift polewards, but not necessarily low clouds (Zelinka et al., 2018). The poleward shift of clouds causes them to prevail in areas that experience less solar radiation. While this was previously thought to induce a positive cloud feedback, the responses to climate change of the different cloud types to this poleward shift seem to cancel each other, thus not inducing any cloud feedback (Forster et al., 2021).

Another negative cloud feedback results from changes in the cloud phase in a warmer climate: If clouds consist of more liquid water instead of ice in a warmer climate, they will have a higher optical depth (Tan et al., 2016; Lohmann and Neubauer, 2018; Hofer et al., 2024). Since cloud droplets are much smaller and much more numerous than ice crystals, a liquid cloud has a larger surface area and hence a higher optical depth for the same water content compared to a pure ice cloud. In addition, liquid clouds precipitate less than clouds containing ice (Mülmenstädt et al., 2015; Heymsfield et al., 2020, Chapter 10), thus their lifetimes are longer, and hence they reflect more solar radiation back to space. This cloud-phase feedback

https://doi.org/10.1017/9781009485654.013 Published online by Cambridge University Press

is rather small and has been assessed to be $-0.03 \pm 0.05\ \mathrm{W\,m^{-2}\,K^{-1}}$ with medium confidence (Forster et al., 2021), but can locally be more important, for example, in polar regions (Tan and Storelvmo, 2019).

In summary, IPCC AR6 concluded that an overall negative cloud feedback is very unlikely. It estimated the net cloud feedback to be $0.42\ \mathrm{W\,m^{-2}\,K^{-1}}$ with a very likely range of -0.1 to $0.94\ \mathrm{W\,m^{-2}\,K^{-1}}$ (Forster et al., 2021), translating into a temperature increase of 0.4 K for a doubling of CO_2 from pre-industrial conditions.

12.3.4 Sum of all Feedbacks

As shown in Figure 12.14, the initial Planck feedback results in a surface temperature increase of 1.2 K. The best estimate of the ECS for a doubling of CO_2 is 3 K (Forster et al., 2021), hence a temperature increase of 1.8 K results from positive feedbacks as follows: the cloud feedback adds 0.4 K, the combined water vapor and lapse rate feedback adds 1.1 K, and the albedo feedback adds 0.3 K (Figure 12.14). Thus, according to eq. (12.3), the overall climate sensitivity parameter λ for a doubling of CO_2, including all feedbacks to a first order, can be estimated as

$$\lambda = \frac{\Delta F_{2\times CO2}}{\mathrm{ECS}} = \frac{3.93\ \mathrm{W\,m^{-2}}}{3\ \mathrm{K}} = 1.31\ \mathrm{W\,m^{-2}\,K^{-1}}. \tag{12.8}$$

If we take the ERF from CO_2 of $2.16\ \mathrm{W\,m^{-2}}$ between 1750 and 2019 (Figure 12.9), this translates to a warming of 1.01 K over this time period, as indicated in Figure 12.10. However, as we have seen in Figure 2.4, the entire warming has not yet been realized and therefore we have the $0.7\ \mathrm{W\,m^{-2}}$ imbalance in the system. If we apply the overall climate sensitivity parameter $\lambda = 1.31\ \mathrm{W\,m^{-2}\,K^{-1}}$ to the CO_2 ERF of $2.16\ \mathrm{W\,m^{-2}}$ between 1750 and 2019, then the equilibrium warming according to eq. (12.3) is $\Delta T_s = \frac{2.16\ \mathrm{W\,m^{-2}}}{1.31\ \mathrm{W\,m^{-2}\,K^{-1}}} = 1.65\ \mathrm{K}$, which means that 0.64 K of the warming is not yet realized. This implies that the warming that is already in the system will cause the temperature to increase above the stricter target of the Paris Agreement[3], which aims to limit global warming to below 1.5 K with respect to pre-industrial times. Therefore, a better measure for climate change at a given moment in time is the *transient climate response* (Otto et al., 2013; Knutti et al., 2017).

12.4 Climate Intervention Involving Aerosol Particles and Clouds

As discussed in Section 12.1, aerosol particles partly offset the greenhouse gas warming by both aerosol-radiation and aerosol–cloud interactions. On this basis, different methods have been suggested to deliberately alter the climate system in order to alleviate the impacts of climate change until mitigations of CO_2 emissions and carbon-removal technologies become sufficiently effective (Jones et al., 2018). Methods that change elements of the climate system are referred to as climate (or geo-) engineering or climate intervention (National Research Council, 2015). While the term geoengineering is mainly used when discussing methods to

[3] www.un.org/en/climatechange/paris-agreement

https://doi.org/10.1017/9781009485654.013 Published online by Cambridge University Press

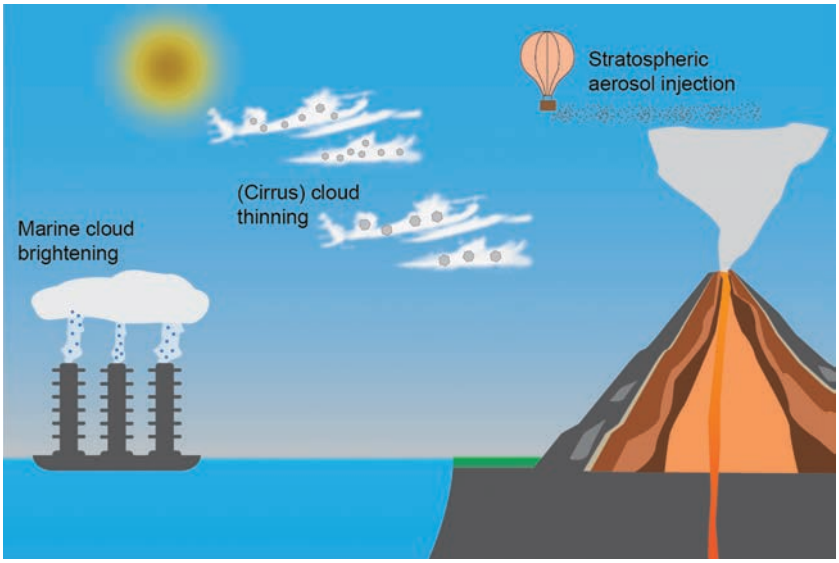


Figure 12.18 Schematic of the climate intervention methods discussed in Section 12.4.

remove CO_2 from the atmosphere, climate intervention focuses on modifying Earth's radiation balance to reduce warming (National Research Council, 2015).

The topic of climate intervention is highly debated in science and politics. As such, we stress that this section is not recommending the use of climate intervention to offset greenhouse gas warming. Rather, we provide an overview of some suggested climate intervention methods.

Specifically, here, we only discuss the physical background of climate intervention methods that affect the radiation balance by deliberate injections of aerosol particles into the atmosphere, as an application of the aerosol–cloud interactions discussed earlier. These methods are referred to as solar radiation management (SRM) or albedo modifications (National Research Council, 2015). They aim at reducing the incoming solar radiation either by injecting aerosol particles into the stratosphere or by enhancing the albedo of marine stratiform clouds, as shown in Figure 12.18. In addition, methods to change the microphysical and radiative properties of ice-containing clouds by injecting INPs has been proposed. These methods affect how cirrus clouds and mixed-phase clouds interact with both shortwave and longwave radiation (Section 12.4.3).

Climate intervention scenarios are typically evaluated against a global warming reference scenario. These scenarios are either specified in terms of abrupt or continuous increases in atmospheric CO_2 concentrations, in terms of so-called *representative concentration pathways* (RCPs) or in terms of SSPs (Meinshausen et al., 2020).

12.4.1 Stratospheric Aerosol Injections

Major volcanic eruptions can directly inject aerosol precursor gases, like SO_2, and particles into the stratosphere. In the stratosphere, the SO_2 is then oxidied to H_2SO_4 and nucleates,

https://doi.org/10.1017/9781009485654.013 Published online by Cambridge University Press

forming submicrometer sulfate aerosol particles (Section 6.5), which then reflect solar radiation, leading to a cooling of Earth's global mean temperature. Therefore, major volcanic eruptions can usually be inferred from the Earth' global mean temperature record.

For instance, the Mt. Pinatubo eruption in June 1991 caused an input of 9.25 ± 2.00 Mt S, initially mainly as gaseous SO_2, into the stratosphere (McCormick et al., 1995; Guo et al., 2004). In the year after its eruption, the global mean surface temperature dropped by 0.5 K as a result of the increased planetary albedo due to the presence of sulfate aerosol particles (Hansen et al., 1992; Soden et al., 2002).

Stratospheric aerosol injection (SAI) is a climate intervention (Figure 12.18) method inspired by this climate impact from volcanic eruptions. It involves injecting aerosol particles into the stratosphere to reflect sunlight and reduce warming. Crutzen (2006) proposed an SRM method in which 5 Mt S yr^{-1} would need to be continuously injected into the stratosphere to offset the radiative forcing from $2 \times CO_2$ of 3.93 W m^{-2} (Forster et al., 2021).

Certainly, cooling of the climate by sulfate particles also occurs by tropospheric sulfate aerosols emitted from, for example, burning of fossil fuels (Figure 12.2). However, increasing tropospheric (sulfate) aerosol mass enhances air pollution and negatively affects human health. A major advantage of injecting (sulfate) aerosol particles into the stratosphere is their long stratospheric lifetime of a couple of years as compared to a few days in the troposphere (Figure 6.15). Consequently, much less sulfate aerosol would be needed in the stratosphere than in the troposphere in order to achieve comparable cooling effects on climate (Dickinson, 1996).

According to GCM studies, an ERF of -8 to -1 W m^{-2} could be achieved with Stratospheric aerosol injection (SAI), depending on the location and amount of stratospheric SO_2 injection (Niemeier and Timmreck, 2015; Visioni et al., 2017; Kleinschmitt et al., 2018; Tilmes et al., 2018). However, Kleinschmitt et al. (2018) obtained at most a -2 W m^{-2} ERF because they found that at higher SO_2 injections, the resulting sulfate aerosol particles start to coagulate and thus settle gravitationally more readily, ultimately reducing their stratospheric lifetime.

While aerosol-based albedo modifications have the potential to reduce climate warming, the major concern with such climate intervention methods is whether they are environmentally safe. Side effects of SAI include, for instance, changes in precipitation pattern (Robock et al., 2009; Lee et al., 2021), resulting from a reduction in the shortwave radiation at the surface, and thus a reduction in the latent heat flux (evaporation) via eq. (2.17). In the global annual mean, evaporation equals precipitation, therefore SAI leads to a reduction in global mean precipitation (Boucher et al., 2013). Furthermore, depending on the latitude of the SAI, the Indian summer monsoon may be reduced by 20–30 % in intensity (Krishnamohan and Bala, 2022). SAI would also cause a change toward more diffuse and less direct solar radiation reaching Earth's surface, with implications for vegetation, especially crop growth (Robock et al., 2009; Lee et al., 2021). Moreover, because heterogeneous chemical reactions on sulfate aerosols can lead to stratospheric ozone destruction (Hanson et al., 1994; Robock et al., 2009; Tilmes et al., 2015), other particles, such as calcite (Keith et al., 2016), alumina (Vattioni et al., 2023), titanium dioxide (Pope et al., 2012), or diamonds (Vattioni et al., 2024) have been proposed as alternatives. Nonetheless, all substances can have side effects, for instance, when settling into the troposphere and affecting cirrus cloud properties (Cziczo et al., 2019).

https://doi.org/10.1017/9781009485654.013 Published online by Cambridge University Press

12.4.2 Marine Cloud Brightening

As discussed in Section 12.1.2 and shown in Figures 1.4f and 12.6, ship emissions into the marine boundary layer can lead to the formation of ship track clouds. However, ship tracks are not visible all the time (Manshausen et al., 2022). Estimates of the ERF of aerosol-related ship emissions from GCMs range between -0.1 and $-0.6\ \mathrm{W\,m^{-2}}$ (Lauer et al., 2007; Peters et al., 2012), but amount only to -0.0004 and $-0.0006\ \mathrm{W\,m^{-2}}$ as estimated from satellite data (Schreier et al., 2007). The International Maritime Organization imposed new regulations in 2020 to limit sulfur emissions from the shipping industry. The global effect of these regulations has been estimated to have reduced IRFaci from shipping emissions by about $0.1\ \mathrm{W\,m^{-2}}$ (Diamond, 2023).

Given that an increase in the amount or reflectivity of marine boundary layer clouds increases the planetary albedo, *marine cloud brightening* (MCB) was put forward by Latham (1990) as another SRM method. MCB requires the injection of aerosol particles that act as CCN and has been investigated in various modeling studies since then (e.g., Wood, 2021). In these studies, the aerosol population below marine low clouds is often augmented by increasing the surface source (flux) of sea salt particles that can act as CCN. In field experiments, small solution droplets containing sea salt would need to be injected into the marine boundary layer, using, for example, wind-driven sprayer boats, as depicted in Figure 12.18. Then the clouds would have a larger cloud droplet number concentration, a higher cloud albedo, and reflect more sunlight.

The IPCC AR6 (Lee et al., 2021) concluded that MCB could cause an ERF of -1 to $-5\ \mathrm{W\,m^{-2}}$, depending on the scale and amount of sea salt CCN injected into the marine boundary layer (Latham et al., 2012; Ahlm et al., 2017; Stjern et al., 2018). Besides the quantity of the injected sea salt CCN, the impact of MCB further depends on where it is deployed, as well as the size, lifetime, and albedo of the unperturbed low marine clouds (Wood, 2021).

Figure 12.19 shows the global mean temperature response of nine GCMs to a 50 % increase in the cloud droplet number concentration of low marine clouds (Stjern et al., 2018). Over the period 2020–2069, all models predicted a statistically significant decrease in global mean surface temperature of -0.96 (-0.17 to -1.21) K in response to MCB relative to the RCP4.5 scenario. This decrease in surface temperature is accompanied by a decrease in the global mean precipitation rate of -2.35 (-0.57 to -2.96) % in the colder climate. However, the change in precipitation rate is not spatially uniform. As MCB increases the land-sea temperature contrast, the rising air motions over land are increased, enhancing land precipitation by 1 % in low latitudes, such as in subtropical Africa, Australia, and South America (Stjern et al., 2018). Figure 12.19 further reveals that when the MCB was terminated in the GCM simulations in the year 2070, the simulated temperatures approached the temperatures of the RCP4.5 scenario within a period of 20 years.

12.4.3 Cloud Thinning

We have seen in Section 2.3 that thin cirrus clouds with low cloud optical depth are semi-transparent to shortwave radiation, allowing most of the solar radiation to be transmitted to

https://doi.org/10.1017/9781009485654.013 Published online by Cambridge University Press

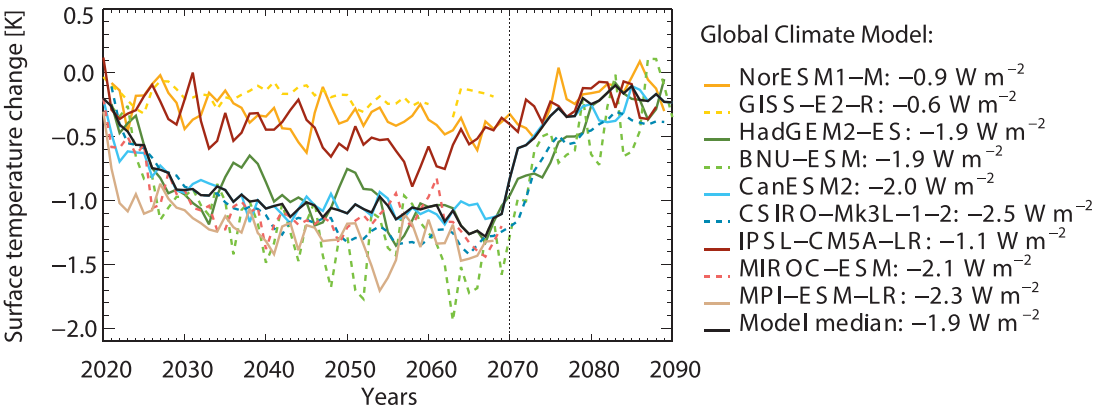


Figure 12.19 Time series of the differences in globally averaged surface temperature between each climate model's RCP4.5 reference simulation and the marine cloud brightening (MCB) simulation in the different colors where the cloud droplet number concentration in low marine clouds was increased by 50 % to counteract the radiative forcing due to greenhouse gas emissions under the RCP4.5 scenario. The dotted vertical line corresponds to the termination of MCB. Figure adapted from Stjern et al. (2018).

the Earth's surface. At the same time, cirrus clouds have low cloud top temperatures and thus emit the absorbed longwave radiation at considerably lower temperatures than Earth's surface, causing a net warming effect. By contrast, in the case of thick cirrus, the relatively higher reflection of shortwave radiation can balance their reduced emission of longwave radiation.

Cirrus cloud thinning (CCT) thus affects both the shortwave and the longwave radiation (Figure 12.18). CCT was put forward by Mitchell and Finnegan (2009) and is based on a GCM study by Lohmann et al. (2008), who evaluated the difference in the TOA radiation balance under the assumption that all cirrus clouds form either purely by heterogeneous ice nucleation on INPs or purely by the homogeneous freezing of solution droplets (Section 9.1). The conditions for the simulations by Lohmann et al. (2008) are depicted in Figures 12.20: The number concentration of mineral dust particles immersed in aqueous solution droplets that can nucleate ice heterogeneously by acting as immersion-freezing INPs (Fr_{imm}^{SD}, orange shading in Figure 9.6) is much lower than the concentration of aqueous solution droplets that can form ice via homogeneous freezing (compare Figures 12.20a and 12.20b). Because the ice crystal number concentration in cirrus formed by heterogeneous ice nucleation is limited by the number concentration of immersed dust particles, it is much lower than that formed by homogeneous ice nucleation (compare Figures 12.20c and 12.20d). The heterogeneously nucleated ice crystals in cirrus clouds can thus grow to larger sizes and sediment faster, decreasing the ice water content and increasing the global mean precipitation rate. Combined with their lower number concentrations, this leads to a reduced cloud optical depth and less reflected solar radiation compared to the homogeneously nucleated cirrus clouds. In the global annual mean, this effect has been estimated to reduce SCRE by 2.7 $W m^{-2}$ (Lohmann et al., 2008).

However, the less negative SCRE is more than offset by reductions in the LCRE of these clouds. Heterogeneous ice nucleation occurs at lower ice supersaturations and higher temperatures than homogeneous ice nucleation (Figures 9.6 and 12.20c,d), which reduces their LCRE (Sections 2.3 and 12.3). In addition, their lower optical depth results in a reduced longwave

https://doi.org/10.1017/9781009485654.013 Published online by Cambridge University Press

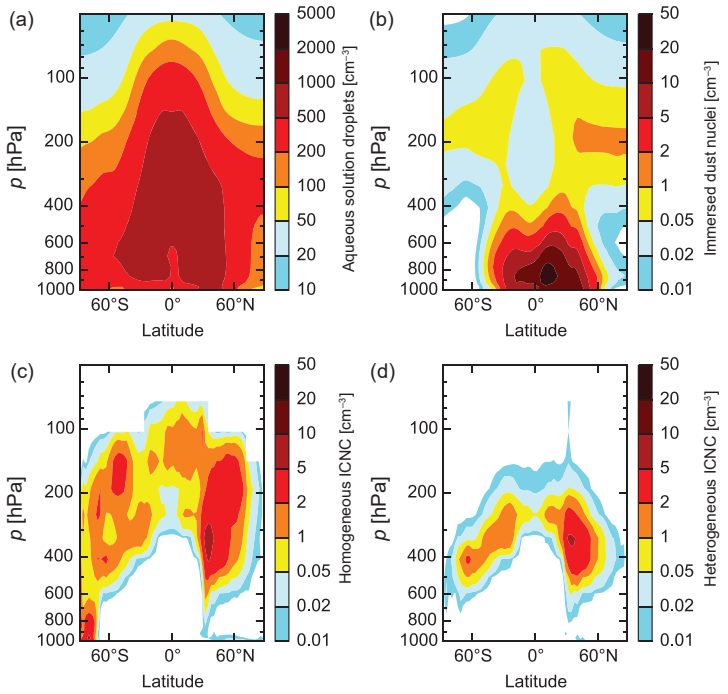


Figure 12.20 Annual zonal mean latitude versus pressure cross-sections of (a) number concentration of aqueous solution droplets, (b) number concentration of dust INPs immersed within aqueous solution droplets, (c) ICNC assuming pure homogeneous ice nucleation, and (d) ICNC assuming pure heterogeneous ice nucleation. Note the different color scale in panel (a). Figure adapted from Lohmann et al. (2008). ©IOP Publishing. Reproduced by permission of IOP Publishing. All rights reserved.

absorptivity, and according to Kirchhoff's law (eq. 2.4), to a reduced longwave emissivity, resulting in an enhanced longwave transmissivity. Thus, the global annual mean LCRE is reduced by $4.7\,\mathrm{W\,m^{-2}}$ and the net CRE is $-2\,\mathrm{W\,m^{-2}}$ for heterogeneously nucleated cirrus clouds (Lohmann et al., 2008). This study illustrates that CCT can lead to a cooling of the Earth-atmosphere system.

The modeling studies by Storelvmo et al. (2013) and Storelvmo and Herger (2014) suggested that a negative CRE of $2\,\mathrm{W\,m^{-2}}$ could be achieved by injecting 18 INPs $\mathrm{L^{-1}}$ (Figure 12.21) into the upper troposphere, confirming the earlier proposal by Mitchell and Finnegan (2009) to inject INPs (bismuth trioxide, BiO_3) into the upper troposphere, specifically into regions that are prone to cirrus formation by homogeneous nucleation. However, whether CCT is successful and how large the negative CRE would be, depends strongly on the number concentration of injected INPs, as shown in Figure 12.21. On the one hand, seeding with too few INPs is not effective because the INP concentration is not large enough to remove the available supersaturation, so the majority of the ice crystals would still nucleate homogeneously (Kärcher and Lohmann, 2003). Seeding with too many INPs, on the other hand, can lead to

https://doi.org/10.1017/9781009485654.013 Published online by Cambridge University Press

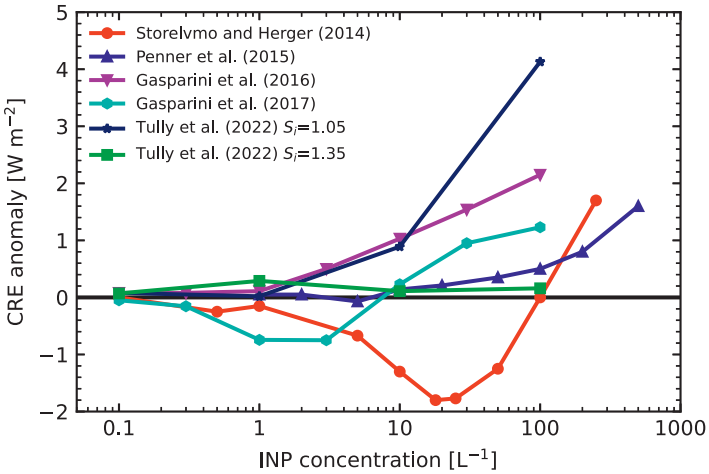


Figure 12.21 Comparison of the global mean Cloud radiative effect (CRE) anomalies at top of the atmosphere (TOA) in response to seeding cirrus with an increasing Ice-nucleating particle (INP) concentration. The data are taken from the studies by Storelvmo and Herger (2014), Penner et al. (2015), Gasparini and Lohmann (2016), Gasparini et al. (2017), Tully et al. (2022). The Tully et al. (2022) study assumed two different saturation ratios with respect to ice ($S_i = 1.05$ and $S_i = 1.35$) at which the INPs nucleate.

cirrus clouds that are more opaque than the unperturbed cirrus. Such overseeding changes the sign of CCT from a net negative to a net positive CRE. Subsequent studies (Penner et al., 2015; Gasparini and Lohmann, 2016; Gasparini et al., 2017; Tully et al., 2022) found CCT to be much less effective than initially suggested by the results of Storelvmo et al. (2013) and Storelvmo and Herger (2014), because in more recent GCM simulations, more unperturbed cirrus were formed by heterogeneous nucleation, resulting in more overseeding. In the studies by Gasparini and Lohmann (2016), Gasparini et al. (2017), and Tully et al. (2022), the additional INP also caused cirrus cloud formation in regions that were previously cloud-free. This effect is especially pronounced if the seeding INPs are assumed to be so ice-active that they trigger ice nucleation already at a supersaturation with respect to ice of $S_i = 1.05$ (Tully et al., 2022). If they are less ice-active and only initiate ice nucleation at $S_i = 1.35$, overseeding is much less pronounced, but the overall effect of CCT is close to zero in that case (Figure 12.21).

Instead of thinning cirrus clouds, Villanueva et al. (2022) suggested thinning mixed-phase clouds in polar regions in winter by injecting INPs. This method aims at inducing the Wegener–Bergeron–Findeisen process (Figure 3.14), which has been exploited in artificial weather modification, for instance, to enhance the snowpack in the Western Rocky Mountains (French et al., 2018; Rauber et al., 2019). Winter has been chosen for mixed-phase cloud thinning because then CRE of mixed-phase clouds is positive. Using a sufficiently large INP concentration to trigger the glaciation of supercooled liquid clouds resulted in a cooling of the Arctic and Southern Oceans by −1 °C and −0.6 °C, respectively (Villanueva et al., 2022).

https://doi.org/10.1017/9781009485654.013 Published online by Cambridge University Press

12.4.4 Summary of the Climate Intervention Discussion

The methods discussed earlier originate from our knowledge about aerosol–cloud interactions using computer simulations (Boucher et al., 2013; Lee et al., 2021). The first trial of MCB with dispersing sea salt aerosols was conducted in 2020 around Australia in an attempt to prevent the further bleaching of the corals in the Great Barrier Reef[4]. While local climate adaptation like this and other potential benefits of offsetting the greenhouse gas warming to some degree may appear attractive, climate engineering in terms of SRM comes with side effects, risks, and costs (Robock et al., 2009; Tilmes et al., 2015; Lee et al., 2021). For a detailed discussion of the SRM methods, their side effects, and technical implementation, the reader is referred to the assessments in IPCC AR5 (Boucher et al., 2013) and AR6 (Lee et al., 2021).

In addition, neither SRM methods nor cloud thinning can compensate ocean acidification due to the increasing atmospheric CO_2 concentration. Certainly, these methods aim purely to treat the symptoms but not to reduce the CO_2 concentration. Moreover, they are accompanied by ethical, governance, and security concerns (Halstead, 2018; Lawrence et al., 2018; Lockley, 2019). Another side effect of these climate intervention methods is that if they are abruptly stopped, the temperature would increase rapidly (*termination effect*) (Boucher et al., 2013; Jones et al., 2013; Lockley, 2019), which would put stress on ecosystems and species that are sensitive to the rate of climate change. Only if climate intervention involving aerosol particles and clouds is accompanied by aggressive greenhouse gas mitigation, it might be possible to avoid transitions across climate thresholds.

[4] www.nature.com/articles/d41586-021-02290-3

https://doi.org/10.1017/9781009485654.013 Published online by Cambridge University Press